J. Fluid Mech. (2002), *vol.* 456, *pp.* 239–275.
DOI: 10.1017/S0022112001007583 Printed in the United Kingdom

The non-Newtonian rheology of dilute colloidal suspensions

By J. BERGENHOLTZ[1], J. F. BRADY[2]† AND M. VICIC[2]‡

[1]Department of Chemistry, Physical Chemistry, Göteborg University, S-412 96 Göteborg, Sweden

[2]Division of Chemistry and Chemical Engineering, California Institute of Technology, Pasadena, CA 91125, USA

(Received 4 December 2000 and in revised form 11 October 2001)

The non-Newtonian rheology is calculated numerically to second order in the volume fraction in steady simple shear flows for Brownian hard spheres in the presence of hydrodynamic and excluded volume interactions. Previous analytical and numerical results for the low-shear structure and rheology are confirmed, demonstrating that the viscosity shear thins proportional to Pe^2, where Pe is the dimensionless shear rate or Péclet number, owing to the decreasing contribution of Brownian forces to the viscosity. In the large Pe limit, remnants of Brownian diffusion balance convection in a boundary-layer in the compressive region of the flow. In consequence, the viscosity shear thickens when this boundary-layer coincides with the near-contact lubrication regime of the hydrodynamic interaction. Wakes are formed at large Pe in the extensional zone downstream from the reference particle, leading to broken symmetry in the pair correlation function. As a result of this asymmetry and that in the boundary-layer, finite normal stress differences are obtained as well as positive departures in the generalized osmotic pressure from its equilibrium value. The first normal stress difference changes from positive to negative values as Pe is increased when the hard-sphere limit is approached. This unusual effect is caused by the hydrodynamic lubrication forces that maintain particles in close proximity well into the extensional quadrant of the flow. The study demonstrates that many of the non-Newtonian effects observed in concentrated suspensions by experiments and by Stokesian dynamics simulations are present also in dilute suspensions.

1. Introduction

The rheology of colloidal suspensions, consisting of submicrometre size particles dispersed in a Newtonian fluid, is an active field of research. This activity stems from the wide variety of colloidal systems and the many settings in which fluid flow plays a key role. Our understanding of the rheological behaviour of colloidal suspensions has benefited from access to exact results on model systems, such as those on dilute suspensions of particles with well-defined interactions in weak flows. As these weak-flow theories for concentrated systems are continually being improved (Brady 1996; Lionberger & Russel 2000), it is important to focus attention on the effect of stronger flows. By strong flows we mean flows in which the non-dimensional shear rate or Péclet number (Pe) is large.

Because of a number of developments, the effect on the bulk rheology of particle

† Author to whom correspondence should be addressed.
‡ Present address: Cyrano Sciences Inc., Pasadena, CA, USA.

concentration and pairwise interactions at small Pe numbers is now well understood for spherical, Brownian particles. Batchelor's (Batchelor & Green 1972; Batchelor 1977) treatment of the dilute limit and extensions thereof, experiments on model suspensions (van der Werff *et al.* 1989*a*; Segre *et al.* 1995; Watanabe *et al.* 1999), and the integration of hydrodynamic interactions in today's computer simulations have been particularly important in this respect. Considerably less is known, however, about the effect of strong flows on the rheological properties of colloidal systems. This is illustrated by the on-going search for the origin of shear thickening or shear dilatancy (Hoffman 1998). This phenomenon has received attention because of the severe restrictions it places on the processing of suspensions of solid particles.

As already mentioned, the theoretical treatment of dilute colloidal suspensions has been a major contributing factor to the present-day understanding of colloid rheology, including such non-Newtonian effects as shear thinning, and of normal stresses. In this work, we will demonstrate that it serves as a similarly useful vehicle for investigating the shear thickening phenomenon, as well as other non-Newtonian effects caused by strong flows. Russel (1980) has discussed the range of validity of the pair-interaction limit. In this context he notes that, although restricted to small concentrations, the rheological behaviour in this limit mimics qualitatively many of the features observed experimentally for concentrated systems. In this work, it will be seen to hold also for the shear thickening phenomenon.

For monodisperse Brownian hard spheres subjected to steady shear flows, the rheological properties depend on only two dimensionless parameters: the particle volume fraction $\phi = \frac{4}{3}\pi n a^3$ and the Péclet number $Pe = 6\pi\eta_s\dot{\gamma}a^3/kT$, defined in terms of the radius a, number density n, solvent viscosity η_s, shear rate $\dot{\gamma}$, and the thermal energy kT. The Péclet number gauges the importance of convection relative to Brownian motion. It sets the degree to which the spatial arrangement of particles – referred to commonly as the microstructure – is distorted owing to the imposed flow field. For small Péclet numbers, the system remains close to equilibrium because the restoring effects of Brownian motion outweigh the effects of convection that force the system out of equilibrium. This limit has been extensively analysed for dilute suspensions, most notably by Batchelor (1977). More recently, Brady & Vicic (1995) have shown that the deformation of the microstructure is formulated as a regular perturbation expansion in the Péclet number up to second order; higher-order terms have to be determined by matched asymptotic expansions. They demonstrate that to second order in Pe, while the viscosity remains Newtonian, the onset of non-Newtonian behaviour is manifest in normal stress differences. Lionberger (1998) has confirmed this finding by a numerical analysis similar to the one we pursue here. Asymptotic analyses of dilute systems have further produced predictions for the shear-induced microstructures and resulting non-Newtonian rheology, including normal stresses, of slender rods in weak flows (Berry & Russel 1987) and electrostatically stabilized suspensions in weak and moderately strong flows (Russel 1978).

Similar progress towards a complete analysis of the high-Péclet-number limit has not been made. Batchelor & Green (1972) demonstrated that in pure straining flows the steady-state spatial arrangement of particles, contained in the pair-distribution function, is spherically symmetrical, which leads to a Newtonian rheology. They proceeded to show that in simple shear flows for $Pe^{-1} = 0$ the pair-distribution function is indeterminate owing to regions of closed streamlines along which a pair of particles orbit one another. To determine the viscosity for such non-Brownian suspensions some additional effect must be introduced that can transport particles across streamlines. For Brownian particle suspensions this problem is intrinsically

circumvented as Brownian diffusion, even though it may be weak compared to convection for large values of the Péclet number, effects this displacement of particles across streamlines.

Brady & Morris (1997) identified analytically a boundary-layer near particle contact where residual Brownian diffusion balances convection. This is a prominent feature of the microstructure in strong shear flows seen in both computer simulations (Phung, Brady & Bossis 1996; Foss & Brady 2000*b*) and experiments (Parsi & Gadala-Maria 1987). Boundary-layer formation is also encountered at low Péclet number in the related situation of high-frequency oscillatory shear flows, where diffusion balances transient convection near particle contact (Lionberger & Russel 1994). For pure straining flow, Brady & Morris showed that even though the pair-distribution function is asymmetric within the boundary-layer, non-Newtonian effects vanish in the limit $Pe \to \infty$, consistent with the conclusion of Batchelor & Green. By introducing extra excluded volume interactions, by which particles are kept at least a minimum distance $2b > 2a$ apart, where a is the particle radius, Brady & Morris extracted a finite second normal stress difference and an isotropic pressure. Hence, the non-Newtonian rheology survives in the $Pe \to \infty$ limit when particles are kept from precise contact. This may appear to be in contradiction to the fact that the boundary-layer thickness scales as aPe^{-1} (Brady & Morris 1997), but can be explained by the stress being proportional to the product of the boundary-layer volume and the probability density it encloses; this product is $O(1)$ in the high-Pe limit as the pair-distribution function scales linearly with Pe in the boundary-layer when $b > a$. Russel (1978) reached a similar conclusion for electrostatically stabilized particles, when long-range electrostatic forces between particles balance convection. The mutual repulsion displaces particles across streamlines, which imparts a non-Newtonian behaviour to the rheology. However, as the repulsion in this case is soft, the flow will inevitably overwhelm the repulsive force for sufficiently large Pe, leaving a Newtonian rheology in the $Pe^{-1} \to 0$ limit.

Two-particle trajectory-based calculations by Zarraga & Leighton (2001) on non-Brownian particle suspensions yield results in excellent accord with those of the asymptotic analysis of Brady & Morris. The high-Pe asymptotes for the normal stress differences and the osmotic pressure in shear flow without hydrodynamic interactions agree with the predicted values. In particular, a finite, negative second normal stress difference survives at high Pe, indicating that the rheology is non-Newtonian, although the first normal stress difference is found to vanish. Additional $Pe^{-1} = 0$ results for the normal stress differences for smaller b/a values are available from the calculations of Wilson & Davis (2000).

In this work, numerical evaluations of the microstructure and rheology are reported for dilute Brownian suspensions subjected to simple shear flow. The results cover essentially the entire range of Péclet numbers, which permits a detailed analysis of both the onset of non-Newtonian rheology near the weak flow limit and the nature of the boundary-layer in the strong flow, high-Pe limit. The analysis is not limited to, but includes also sheared hard-sphere suspensions in the presence and absence of hydrodynamic interactions. The effect of additional repulsive interactions is investigated in the same way as in Brady & Morris, by including a hard repulsion at a distance $2b > 2a$.

In what follows, the general framework used for the determination of the microstructure and rheology of colloidal suspensions is reviewed in § 2. It consists of the formulation of a two-particle Smoluchowski equation which governs the non-equilibrium pair-distribution function. The stress tensor is evaluated subsequently in

§ 3 by ensemble averaging of the particle stresslets. Section 4 contains a description of the numerical solution methods employed for solving the Smoluchowski equation. In § 5, the weak-flow limit is treated in detail to demonstrate the accuracy of the numerical solutions, as well as to focus on the onset of the non-Newtonian shear rheology signalled by shear-thinning and finite normal stress differences. Emphasis is also placed on the structure of the high-shear boundary layer, which plays a dominant role in determining the rheology. Results are shown for several excluded volume parameters b/a, which are useful in that they provide qualitative trends for the shear rheology of suspensions containing particles interacting via short- and longer-range repulsive interactions. However, as demonstrated by Russel (1978) for realistic soft repulsions, particle pairs accumulate at characteristic distances that are governed by the competition between the repulsion and convection. As a consequence, an effective hard-sphere radius (b/a) will depend on the magnitude and range of the repulsion as well as on the strength of the flow. This finding is indeed well established by experiments (Mewis *et al.* 1989). Nevertheless, by limiting this study to hard-core repulsions, we can provide results in terms of just two parameters, b/a and Pe. Thus by varying b/a the interaction can be tuned, so that we can examine both the hydrodynamically dominated ($b/a \sim 1$) regime and the regime dominated by Brownian motion and interparticle forces ($b/a \to \infty$); the latter two we will collectively refer to as thermodynamic forces. A noteworthy finding is that the level of shear thickening can be controlled by the inclusion or exclusion of hydrodynamic interactions by varying b/a.

2. Non-equilibrium microstructure

When N suspended particles in a volume V are subjected to a constant velocity gradient $\boldsymbol{\Gamma}$, the probability density for the particle coordinates $P_N(\boldsymbol{x}^N, t)$ satisfies the Smoluchowski equation

$$\frac{\partial P_N}{\partial t} + \boldsymbol{\nabla} \cdot \boldsymbol{j}_N = 0, \tag{2.1}$$

with the $3N$-dimensional particle flux vector given by

$$\boldsymbol{j}_N = \boldsymbol{U} P_N + \boldsymbol{R}_{FU}^{-1} \cdot (\boldsymbol{F}^P - kT \boldsymbol{\nabla} \ln P_N) P_N. \tag{2.2}$$

In the above, $\boldsymbol{U}$ is the hydrodynamic velocity vector and $\boldsymbol{F}^P = -\boldsymbol{\nabla} V_N$ is the direct force vector which derives from an N-particle interaction potential V_N. The hydrodynamic mobility tensors $\boldsymbol{R}_{FU}^{-1}$ relate the forces to the resulting velocities. At equilibrium ($\boldsymbol{U} = 0$) the probability distribution is independent of time and the net flux vanishes $\boldsymbol{j}_N = \boldsymbol{0}$. The particle mobilities disappear from the governing equation ($\boldsymbol{R}_{FU}^{-1}$ is positive definite), leaving a balance between the conservative forces and gradients in the probability distribution

$$\boldsymbol{F}^P = kT \boldsymbol{\nabla} \ln P_N^0. \tag{2.3}$$

This equation is solved by the Boltzmann distribution $P_N^0 = \exp(-V_N/kT)/Z_N$, where Z_N is the configurational integral which guarantees that the probability density is normalized.

Forcing the fluid to flow causes relative motion among particles. For a linear flow the macroscopic velocity gradient $\langle \boldsymbol{\Gamma} \rangle = \langle \boldsymbol{E} \rangle + \langle \boldsymbol{\Omega} \rangle$ is a superposition of pure straining motion, characterized by the symmetric rate-of-strain tensor $\langle \boldsymbol{E} \rangle$, and pure rotation, characterized by the anti-symmetric vorticity tensor $\langle \boldsymbol{\Omega} \rangle$. The particle velocities that

result from the linear flow are given by

$$\boldsymbol{U} = \langle \boldsymbol{\Gamma} \rangle \cdot \boldsymbol{x} + \boldsymbol{R}_{FU}^{-1} \cdot \boldsymbol{R}_{FE} : \langle \boldsymbol{E} \rangle. \tag{2.4}$$

The first term arises simply from the advection of the particles by the flow. The second term originates from the hydrodynamic interactions among particles. The additional hydrodynamic resistance tensor $\boldsymbol{R}_{FE}$ indicates that hydrodynamic forces are exerted on the particles as a result of the imposed flow. In the absence of hydrodynamic interactions $\boldsymbol{R}_{FE} = \boldsymbol{0}$ and the velocity vector is given simply by $\boldsymbol{U} = \langle \boldsymbol{\Gamma} \rangle \cdot \boldsymbol{x}$.

This work focuses on steady shear flows for which the probability distribution is independent of time, but deviates from the equilibrium Boltzmann distribution. Moreover, the analysis will be restricted to the dilute limit where only pairs of particles need be considered. The motivation for this simplification is that principally exact results can be obtained for the non-equilibrium pair-distribution function, even for strong flows. Special attention will be given to the competition between thermodynamic (effective Brownian and interparticle) forces and hydrodynamic forces. For this reason, a convenient way of tuning the relative importance of thermodynamic and hydrodynamic interactions is required. Such a device can be realized by introducing an excluded volume interaction, often referred to as an effective hard-sphere interaction or an excluded annulus model, of the form

$$V(r) = \begin{cases} \infty & (r < 2b/a), \\ 0 & (r > 2b/a), \end{cases} \tag{2.5}$$

where r has been made dimensionless momentarily with the hard core radius a. We shall later adopt b as the length scale in all subsequent normalizations. When $b/a = 1$, the system consists of hard spheres interacting hydrodynamically with each other, whereas on approaching the limit $b/a \to \infty$, the particles are kept apart such that they no longer experience any hydrodynamic interaction; as a consequence, the special case of sheared hard-sphere suspensions under neglect of hydrodynamic interactions is recovered. The effective hard-sphere model is widely used in colloid science and in the modelling of the rheology of suspensions (Russel 1984; Mewis *et al.* 1989; Russel, Saville & Schowatter 1989). Far more recently, it has been adopted as a model of surface roughness in non-colloidal suspensions (Wilson & Davis 2000). The influence of other aspects of the interparticle interaction on the structure and rheology, such as soft repulsions and attractive interactions, are left for future analyses.

The equation governing the pair-distribution function is obtained by integrating the steady N-particle Smoluchowski equation over all the particle positions but two and neglecting any three-body couplings. The result is the steady two-particle Smoluchowski equation, given by

$$\nabla_r \cdot \boldsymbol{D}_r \cdot \nabla_r g(\boldsymbol{r}) = Pe_b \nabla_r \cdot (\boldsymbol{U}_r g(\boldsymbol{r})), \tag{2.6}$$

where all lengths have been made dimensionless with the excluded volume radius b, and a relative coordinate system has been chosen with $\boldsymbol{r} = \boldsymbol{x}_2 - \boldsymbol{x}_1$ and $\nabla_r = \partial/\partial \boldsymbol{r}$. Moreover, the relative diffusivity $\boldsymbol{D}_r$, here dimensionless on the isolated particle, Stokes–Einstein diffusivity $D_0 = kT/6\pi\eta_s a$, is defined by $\boldsymbol{D}_r = \boldsymbol{D}_{22} + \boldsymbol{D}_{11} - \boldsymbol{D}_{12} - \boldsymbol{D}_{21}$. The relative velocity $\boldsymbol{U}_r = \boldsymbol{U}_2 - \boldsymbol{U}_1$ is non-dimensional on $b\dot{\gamma}$, where $\dot{\gamma}$ is the magnitude of the velocity gradient and $n^2 g(\boldsymbol{r}) = ((N-2)!)^{-1} \int \mathrm{d}\boldsymbol{x}_3 \ldots \mathrm{d}\boldsymbol{x}_N P_N$.

Note that because (2.6) applies in the region $r = |\boldsymbol{r}| > 2$, $\nabla_r V(r) = 0$, and (2.6) expresses a balance between Brownian motion (left-hand side of (2.6)) and convection (right-hand side of (2.6)). On the one hand, convection by the imposed flow drives the system from equilibrium, but on the other hand the external forcing must compete

with Brownian motion which tends to restore equilibrium. The degree to which the structure is perturbed away from equilibrium is determined by the dimensionless Péclet number $Pe_b = b^2\dot{\gamma}/D_0$, which appears naturally in (2.6). The Péclet number can be viewed as a ratio of time scales: the diffusive time b^2/D_0 divided by the convective time scale $1/\dot{\gamma}$; or, equally well, it can be viewed as a ratio of forces: the convective force $\zeta_0(b\dot{\gamma}) = 6\pi\eta_s ab\dot{\gamma}$ divided by the effective Brownian force kT/b.

Following the convention of Batchelor (1977), the relative diffusivity and velocity are expressed in terms of two-body, scalar hydrodynamic functions as

$$\boldsymbol{D}_r = 2[G(r)\hat{\boldsymbol{r}}\hat{\boldsymbol{r}} + H(r)(\boldsymbol{I} - \hat{\boldsymbol{r}}\hat{\boldsymbol{r}})], \tag{2.7}$$

$$\boldsymbol{U}_r = \langle\hat{\boldsymbol{\Gamma}}\rangle \cdot \boldsymbol{r} - \boldsymbol{r} \cdot \langle\hat{\boldsymbol{E}}\rangle \cdot [A(r)\hat{\boldsymbol{r}}\hat{\boldsymbol{r}} + B(r)(\boldsymbol{I} - \hat{\boldsymbol{r}}\hat{\boldsymbol{r}})], \tag{2.8}$$

where $\langle\hat{\boldsymbol{\Gamma}}\rangle = \dot{\gamma}^{-1}\langle\boldsymbol{\Gamma}\rangle$, $\langle\hat{\boldsymbol{E}}\rangle = \dot{\gamma}^{-1}\langle\boldsymbol{E}\rangle$, $\hat{\boldsymbol{r}} = \boldsymbol{r}/r$, and $\boldsymbol{I}$ is the unit dyadic. The hydrodynamic functions $G(r)$ and $H(r)$ describe the relative mobility parallel and transverse to the line of centres of a pair of spheres, whereas $A(r)$ and $B(r)$ relate the relative velocity parallel and transverse to the line of centres to the strain rate.

To completely specify the microstructure, (2.6) is supplemented with boundary conditions. When $r = 2$, the radial component of the relative flux vanishes because of (2.5), which is expressed as

$$\hat{\boldsymbol{r}} \cdot \boldsymbol{D}_r \cdot \nabla_r g(\boldsymbol{r}) = Pe_b \hat{\boldsymbol{r}} \cdot \boldsymbol{U}_r g(\boldsymbol{r}), \tag{2.9}$$

and at large separations

$$g(\boldsymbol{r}) \to 1 \quad \text{as} \quad r \to \infty \tag{2.10}$$

guarantees a structure without long-range order.

Since the non-equilibrium pair-distribution function approaches unity at large distances, it is convenient to introduce the structural deformation function $f(\boldsymbol{r}) = g(\boldsymbol{r}) - 1$. Moreover, since the dilute-limit equilibrium solution for $g(\boldsymbol{r})$ is unity everywhere for $r > 2$, $f(\boldsymbol{r})$ is the departure from the equilibrium microstructure resulting from the imposed flow.

3. Bulk stress

At low Reynolds number, the bulk stress of a colloidal suspension can be written as

$$\langle\boldsymbol{\Sigma}\rangle = -\langle p\rangle\boldsymbol{I} + 2\eta_s\langle\boldsymbol{E}\rangle + \langle\boldsymbol{\Sigma}_P\rangle, \tag{3.1}$$

where $\langle p\rangle$ is the constant fluid pressure, which is indeterminate for an incompressible solvent, and $2\eta_s\langle\boldsymbol{E}\rangle$ is the Newtonian solvent contribution to the deviatoric stress. In addition to the solvent contributions, the colloidal particles generate both isotropic and deviatoric stresses in the fluid by a number of mechanisms, all of which are collected in the particle stress $\langle\boldsymbol{\Sigma}_P\rangle$. This excess stress term is divided into kinetic, $-nkT\boldsymbol{I}$, hydrodynamic, $n\langle\boldsymbol{S}^H\rangle$, Brownian, $n\langle\boldsymbol{S}^B\rangle$, and interparticle, $n\langle\boldsymbol{S}^P\rangle$, contributions as

$$\langle\boldsymbol{\Sigma}_P\rangle = -nkT\boldsymbol{I} + n(\langle\boldsymbol{S}^H\rangle + \langle\boldsymbol{S}^B\rangle + \langle\boldsymbol{S}^P\rangle), \tag{3.2}$$

with

$$\langle\boldsymbol{S}^H\rangle = -\langle\boldsymbol{R}_{SU} \cdot \boldsymbol{R}_{FU}^{-1} \cdot \boldsymbol{R}_{FE} - \boldsymbol{R}_{SE}\rangle : \langle\boldsymbol{E}\rangle, \tag{3.3}$$

$$\langle\boldsymbol{S}^B\rangle = -kT\langle\nabla \cdot (\boldsymbol{R}_{SU} \cdot \boldsymbol{R}_{FU}^{-1})\rangle, \tag{3.4}$$

$$\langle\boldsymbol{S}^P\rangle = -\langle(x\boldsymbol{I} + \boldsymbol{R}_{SU} \cdot \boldsymbol{R}_{FU}^{-1}) \cdot \boldsymbol{F}^P\rangle, \tag{3.5}$$

where $\langle \ldots \rangle$ denotes the ensemble average $(N!)^{-1}\int \mathrm{d}\boldsymbol{x}^N P_N \ldots$, which involves the non-equilibrium probability density found from solving (2.1).

Integration of (3.3)–(3.5) over all but two particle positions and neglect of three-body terms results in the following expressions, valid for $b > a$, for the three contributions to the particle stress:

$$n\langle \boldsymbol{S}^H \rangle = 5\phi\eta_s\dot{\gamma}\langle \hat{\boldsymbol{E}} \rangle + 5\phi^2\eta_s\dot{\gamma}\langle \hat{\boldsymbol{E}} \rangle + \frac{15}{4\pi}\phi_b^2\left(\frac{a}{b}\right)^3\eta_s\dot{\gamma}\int \mathrm{d}\boldsymbol{r}g(\boldsymbol{r}) \times \left\{K(r)\langle \hat{\boldsymbol{E}} \rangle + L(r)\left(\hat{\boldsymbol{r}}\cdot\langle \hat{\boldsymbol{E}} \rangle\hat{\boldsymbol{r}} + \langle \hat{\boldsymbol{E}} \rangle\cdot\hat{\boldsymbol{r}}\hat{\boldsymbol{r}} - \tfrac{2}{3}\boldsymbol{I}\left(\hat{\boldsymbol{r}}\cdot\langle \hat{\boldsymbol{E}} \rangle\cdot\hat{\boldsymbol{r}}\right)\right) + M(r)\left(\hat{\boldsymbol{r}}\cdot\langle \hat{\boldsymbol{E}} \rangle\cdot\hat{\boldsymbol{r}}\right)\left(\hat{\boldsymbol{r}}\hat{\boldsymbol{r}} - \tfrac{1}{3}\boldsymbol{I}\right) - \tfrac{2}{5}\mathscr{B}(r)\boldsymbol{I}\left(\hat{\boldsymbol{r}}\hat{\boldsymbol{r}} - \tfrac{1}{3}\boldsymbol{I}\right)\right\}, \tag{3.6}$$

$$n\langle \boldsymbol{S}^B \rangle = -\frac{3nkT\phi_b}{8\pi}\int \mathrm{d}\boldsymbol{r}g(\boldsymbol{r})W(r)\left(\hat{\boldsymbol{r}}\hat{\boldsymbol{r}} - \tfrac{1}{3}\boldsymbol{I}\right) - \frac{nkT\phi_b}{6\pi}\frac{a}{b}\boldsymbol{I}\int \mathrm{d}\boldsymbol{r}\mathscr{A}(r)\frac{\partial g(\boldsymbol{r})}{\partial r}, \tag{3.7}$$

$$n\langle \boldsymbol{S}^P \rangle = -\frac{3nkT\phi_b}{\pi}(1 - A(2))\int \mathrm{d}\Omega g(2\hat{\boldsymbol{r}})\left(\hat{\boldsymbol{r}}\hat{\boldsymbol{r}} - \tfrac{1}{3}\boldsymbol{I}\right) - \frac{nkT\phi_b}{\pi}\boldsymbol{I}\int \mathrm{d}\Omega g(2\hat{\boldsymbol{r}}). \tag{3.8}$$

Here, $K(r)$, $L(r)$, $M(r)$, $W(r)$, $\mathscr{A}(r)$ and $\mathscr{B}(r)$ are additional hydrodynamic functions that result from the decomposition of the two-particle resistance tensors derived from those in (3.3)–(3.5). From the solution of (2.6), the viscometric functions can be calculated from the above stress expressions. For simple shear flow the velocity gradient is defined as $\langle \boldsymbol{\Gamma} \rangle = \dot{\gamma}\hat{\boldsymbol{z}}\hat{\boldsymbol{x}}$ with the flow in the $\hat{\boldsymbol{z}}$-direction, the gradient in the $\hat{\boldsymbol{x}}$-direction, and the vorticity axis directed along $\hat{\boldsymbol{y}}$. The non-Newtonian flow behaviour is characterized by the shear viscosity, $\eta = \Sigma_{xz}/\dot{\gamma}$, and by the first and second normal stress differences

$$N_1 = \Sigma_{zz} - \Sigma_{xx}, \tag{3.9}$$

$$N_2 = \Sigma_{xx} - \Sigma_{yy}. \tag{3.10}$$

Moreover, the flow distorts the equilibrium microstructure which affects the trace of the particle stress. At equilibrium the trace of the particle stress is directly related to the osmotic pressure (Brady 1993) as

$$\Pi_0 = -\tfrac{1}{3}\boldsymbol{I} : \langle \boldsymbol{\Sigma}_P \rangle = nkT(1 + 4\phi_b), \tag{3.11}$$

valid for (2.5). Here, $\phi_b = \frac{4}{3}\pi b^3 n$ is the volume fraction based on the excluded volume radius b. Under flow the isotropic stress changes, and we extend the definition of the osmotic pressure to finite Pe via $\Pi(Pe) = -\frac{1}{3}\boldsymbol{I} : \langle \boldsymbol{\Sigma}_P(Pe) \rangle$. In this work we will refer to this quantity as the shear-dependent osmotic pressure.

Because of the definition adopted in (3.7) for the Brownian stress, the equilibrium osmotic pressure is determined by the interparticle contribution to the particle stress. For a hard-sphere suspension with $b \equiv a$ it is more appropriate to derive the osmotic pressure mechanically. The equilibrium osmotic pressure then arises from the trace of the Brownian particle stress only (Brady 1993). As discussed in Appendix A, the term in the Brownian stress that determines the hard-sphere equilibrium osmotic pressure does not appear in (3.7) because it vanishes when $b > a$ and is replaced by the last term in (3.8). This is a mere matter of definition, as defining the hard-sphere osmotic pressure thermodynamically from the average of the virial, as done here, or mechanically as done previously, yields the identical result because of the asymptotic near-field properties of the hydrodynamic tensors (Jeffrey, Morris & Brady 1993; Brady 1993).

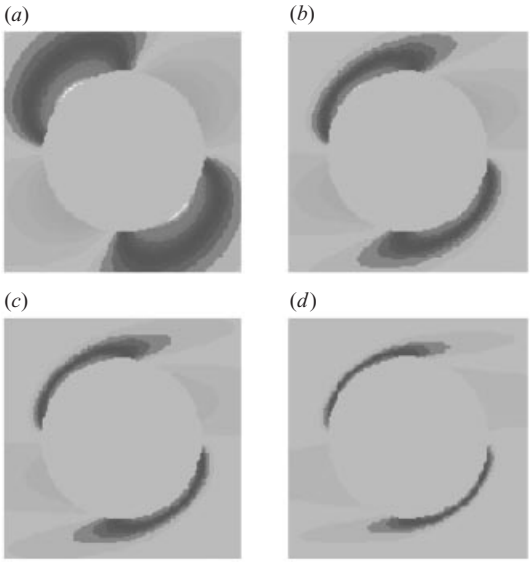

FIGURE 1. The non-equilibrium pair-distribution function $f(\boldsymbol{r}) = g(\boldsymbol{r}) - 1$ in the shear flow-gradient plane as a function of Pe for hard spheres in the absence of hydrodynamic interactions. (*a*) $Pe = 1$, (*b*) 5, (*c*) 10, (*d*) 20.

4. Numerical solution

Obtaining the solution to (2.6) for all Péclet numbers is a challenging problem because of the formation of a boundary-layer on the compressive axes and a wake downstream on the extensional axes. The boundary-layer is a prominent feature of the microstructure in strong shear flows observed in both computer simulations (Phung *et al.* 1996; Foss & Brady 2000*b*) and experiments (Parsi & Gadala-Maria 1987). Figure 1 shows the microstructure in the plane of shear for hard spheres under neglect of hydrodynamic interactions in a simple shear flow; the formation of the boundary-layer is clearly evident and is accompanied by the growth of a wake downstream from the reference particle at the origin. The transport of particles from upstream locations is hindered by the impenetrability of the reference particle, and thus as the Péclet number is increased there is a greater probability of finding particles on the upstream side of the reference particle. Here, the action of the flow is to compress particle pairs, whereas downstream from the reference particle the shear flow exerts an extensional force separating particle pairs. At high Péclet numbers, the boundary-layer is seen to separate from particle contact and enter the bulk along downstream trajectories that outline the wake. The emergence of such wakes, or shadow zones, in strong flows is well known, and the microstructure of a strongly sheared suspension is captured well by the schematic suggested early on by Russel *et al.* (1989, p. 490).

To capture this evolving behaviour two approaches were used to solve (2.6) for the pair-distribution function, or, more conveniently, for the structural deformation $f(\boldsymbol{r}) = g(\boldsymbol{r}) - 1$. For Pe_b up to $O(1)$, a surface spherical harmonic expansion of $f(\boldsymbol{r})$, similar to that used by Lionberger (1998), is employed, whereas for $Pe_b \geqslant 2$ the solution is obtained by a finite-difference method. In order for an expansion method, such as the surface spherical harmonic expansion, to capture the behaviour seen in figure 1, it must be of high order, which proves to be computationally very expensive.

For strong flows, finite-difference methods were found to be more amenable for numerically evaluating the complex microstructures at large Pe_b, including the rapid variation of $f(\boldsymbol{r})$ near $r = 2$ and the growing downstream wake.

The surface spherical harmonic expansion proceeds by defining the expansion coefficients B_{lm} by

$$f(\boldsymbol{r}; Pe_b) = \sum_{l,|m|\leqslant l} B_{lm}(r; Pe_b) Y_{lm}(\theta, \varphi), \tag{4.1}$$

where $Y_{lm}(\theta, \varphi)$ is the surface spherical harmonic defined as

$$Y_{lm}(\theta, \varphi) = \left(\frac{2l+1}{4\pi} \frac{(l-|m|)!}{(l+|m|)!} \right)^{1/2} P_l^{|m|}(\cos\theta) \mathrm{e}^{\mathrm{i}m\varphi}, \tag{4.2}$$

with the associated Legendre polynomial

$$P_l^{|m|}(x) = (1-x^2)^{m/2} \frac{\mathrm{d}^m P_l(x)}{\mathrm{d}x^m}, \tag{4.3}$$

where $P_l(x)$ is the lth Legendre polynomial.

The expansion for $f(\boldsymbol{r})$ is substituted in the Smoluchowski equation (2.6) and the boundary conditions (2.9) and (2.10), which results in a series of coupled ordinary differential equations after use of the orthogonality property of the spherical harmonics, $\int \mathrm{d}\Omega Y_{lm} Y_{pq}^* = \delta_{lp}\delta_{mq}$. Here, Y_{lm}^* is the complex conjugate of Y_{lm} and δ_{ij} is the Kronecker delta function. The ordinary differential equations governing the expansion coefficients $B_{lm}(r; Pe_b)$ take the following form

$$\begin{aligned} G(r)\frac{\mathrm{d}^2 B_{pq}}{\mathrm{d}r^2} + \left(2\frac{G(r)}{r} + \frac{\mathrm{d}G(r)}{\mathrm{d}r} \right) \frac{\mathrm{d}B_{pq}}{dr} - \frac{p(p+1)}{r^2} H(r) B_{pq} \\ = \tfrac{1}{2} Pe_b W(r) \beta_1 + \tfrac{1}{2} Pe_b \sum_{l,|m|\leqslant l} \left\{ \left(W(r) B_{lm} + r(1-A(r)) \frac{\mathrm{d}B_{lm}}{\mathrm{d}r} \right) \beta_2 \right. \\ \left. + (1-B(r))(\beta_3+\beta_4) B_{lm} + (\beta_5+\beta_6) B_{lm} \right\}, \end{aligned} \tag{4.4}$$

with the no-flux boundary condition, evaluated at $r = 2$, as

$$G(r)\frac{\mathrm{d}B_{pq}}{\mathrm{d}r} = Pe_b(1-A(r)) \left(\beta_1 + \beta_2 \sum_{l,|m|\leqslant l} B_{lm} \right), \tag{4.5}$$

and the far field, no deformation boundary condition

$$B_{pq} \to 0 \quad \text{as} \quad r \to \infty. \tag{4.6}$$

The constants, β_i with $i = 1, \ldots, 6$, depend on l, m, p and q, and consequently, the ordinary differential equations in (4.4) are coupled. In addition, the constants depend on the specific flow-type, and they are defined as

$$\beta_1 = \int \mathrm{d}\Omega (\hat{\boldsymbol{r}} \cdot \langle \hat{\boldsymbol{E}} \rangle \cdot \hat{\boldsymbol{r}}) Y_{pq}^*, \tag{4.7}$$

$$\beta_2 = \int \mathrm{d}\Omega (\hat{\boldsymbol{r}} \cdot \langle \hat{\boldsymbol{E}} \rangle \cdot \hat{\boldsymbol{r}}) Y_{lm} Y_{pq}^*, \tag{4.8}$$

$$\beta_3 = \int \mathrm{d}\Omega (\hat{\boldsymbol{r}} \cdot \langle \hat{\boldsymbol{E}} \rangle \cdot \hat{\theta}) \frac{\partial Y_{lm}}{\partial \theta} Y_{pq}^*, \tag{4.9}$$

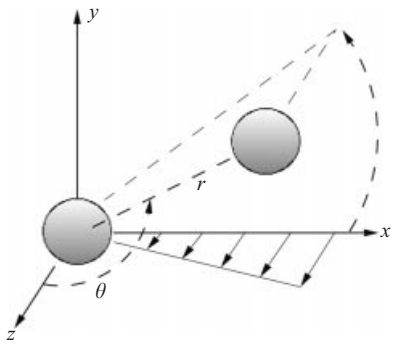

FIGURE 2. Spherical coordinate system with the somewhat unconventional choice of the flow in the z-direction and the gradient along the x-direction.

$$\beta_4 = \int \mathrm{d}\Omega(\hat{\boldsymbol{r}} \cdot \langle \hat{\boldsymbol{E}} \rangle \cdot \hat{\varphi}) \frac{1}{\sin\theta} \frac{\partial Y_{lm}}{\partial \varphi} Y^*_{pq}, \tag{4.10}$$

$$\beta_5 = \int \mathrm{d}\Omega(\hat{\boldsymbol{r}} \cdot \langle \hat{\boldsymbol{\Omega}} \rangle \cdot \hat{\theta}) \frac{\partial Y_{lm}}{\partial \theta} Y^*_{pq}, \tag{4.11}$$

$$\beta_6 = \int \mathrm{d}\Omega(\hat{\boldsymbol{r}} \cdot \langle \hat{\boldsymbol{\Omega}} \rangle \cdot \hat{\varphi}) \frac{1}{\sin\theta} \frac{\partial Y_{lm}}{\partial \varphi} Y^*_{pq}. \tag{4.12}$$

In the above, $\hat{\theta}$ and $\hat{\varphi}$ are unit vectors in the θ- and φ-directions in the spherical coordinate system shown in figure 2. The angular derivatives are evaluated analytically from (4.2) and (4.3).

The number of equations in (4.4) are reduced by noting that $f(\boldsymbol{r})$ must be a real-valued function, requiring that the expansion coefficients satisfy $B_{lm} = B_{l,-m}$. Furthermore, for the simple shear flow in the present analysis, with $\langle \hat{\boldsymbol{\Gamma}} \rangle = \hat{\boldsymbol{z}}\hat{\boldsymbol{x}}$, a further simplification arises because of the symmetry of the flow: $B_{lm} = 0$ when l is odd. The integrals for β_1–β_6 in (4.7)–(4.12) are evaluated analytically with respect to φ and numerically with respect to θ, using the properties of products of associated Legendre polynomials and powers of $\sin\theta$ and $\cos\theta$ (McQuarrie 1983; Vicic 1999).

The remaining ordinary differential equations for the expansion coefficients in (4.4) are solved numerically by approximating them by finite differences. Prior to this step, the radial domain is transformed from $r \in [2, \infty]$ to $t \in [0, 1]$ by introducing the radial variable $t = 2/r$. This transformation permits the far field boundary condition to be rigorously enforced since it is now moved to the finite domain at $t = 0$. This procedure avoids any ambiguities associated with having to apply the far field boundary condition at finite separations as done in a previous numerical solution of the two-particle Smoluchowski equation (Lionberger 1998).

The ordinary differential equations are solved on a uniformly discretized t-grid with an $O(\Delta t^4)$ finite-difference scheme. This scheme results in a band diagonal matrix, the inverse of which is used to obtain the coefficients B_{lm} for an arbitrary choice of the maximum value of l, denoted by l_{max}, in the expansion of $f(\boldsymbol{r})$. The band diagonal matrix is solved by a direct LU-decomposition method (Press *et al.* 1992). The advantage of using a direct method, as opposed to an iterative method, in evaluating the inverse of the band diagonal matrix is that it avoids the convergence problems generally encountered with iterative methods applied to the solution of the Smoluchowski equation at large Pe_b. The penalty is the large, internal memory requirement for storing the matrix, which contains a large number of null entries. As

a consequence, solutions can only be realized in practice for $l_{max} = 14$ when the radial grid consists of 400 nodes because of the prohibitive size of the band diagonal matrix. On the other hand, because the solution method is direct, solutions for any Pe_b can be obtained. Naturally, as $Pe_b \to \infty$ such solutions of the truncated set of differential equations are not accurate as the true solution requires, in principle, $l_{max} \to \infty$ as $Pe_b \to \infty$. Owing to this limitation on the value of l_{max}, only results that lie within 0.1% of those calculated using $l_{max} + 2$ are shown.

To solve the Smoluchowski equation accurately at higher Pe_b it is necessary to resolve the detailed structure of the boundary-layer while maintaining sufficient resolution in the far field to capture the behaviour of the growing wake region (see figure 1). This poses a problem for any numerical solution method because the boundary-layer thickness scales as Pe_b^{-1}, whereas the range of the wake increases linearly with Pe_b (Brady & Morris 1997). In this work the Smoluchowski equation in the interval $2 \leqslant Pe_b \leqslant 200$ is approximated by a finite-difference equation discretized on a grid which places a large number of nodes in the boundary-layer but maintains nodes, albeit sparsely placed, in the far field. As with the spherical harmonic expansion – although now the angular derivatives are handled also with the finite-difference method – the inverse of a sparse matrix must be determined (Press *et al.* 1992). In this case, a lower-order, centred-difference approximation (derivatives with respect to the the azimuthal angle were approximated by forward-differences) was used because the matrix is considerably larger owing to the incorporation of the angular dependence. The matrix of coefficients is tridiagonal with fringes, and it was inverted by a rapid back-substitution algorithm for tridiagonal matrices (Press *et al.* 1992) with corrections due to the fringes determined by iteration (Ng 1974).

The convergence of the iteration becomes progressively slower with increasing Pe_b. For $Pe_b \sim 300$, it no longer converges, necessitating an alternative approach. Since the rheological properties at large Pe are strongly dependent on the behaviour of the boundary layer (Brady & Morris 1997; Vicic 1999), an equation approximating the Smoluchowski equation in the boundary layer, formulated in Appendix B, is solved. In this way the details of the boundary layer are kept at the expense of obtaining the correct far-field behaviour. The resulting boundary-layer equation for $g(\boldsymbol{r})$ is (cf. (B 4))

$$G\frac{\partial^2 g}{\partial y^2} + Q\frac{\partial g}{\partial y} + \frac{HPe_b^{-2}}{4\sin\theta}\left(\frac{\partial}{\partial\theta}\left(\sin\theta\frac{\partial g}{\partial\theta}\right) + \frac{1}{\sin\theta}\frac{\partial^2 g}{\partial\varphi^2}\right) = \frac{Pe_b^{-1}}{2}\left(gW\gamma_r + (\gamma_\theta - Be_\theta)\frac{\partial g}{\partial\theta} + \frac{(\gamma_\varphi - Be_\varphi)}{\sin\theta}\frac{\partial g}{\partial\varphi}\right), \quad (4.13)$$

where $y = Pe_b(r-2)$, $Q = \mathrm{d}G/\mathrm{d}y + GPe_b^{-1}(1 - \frac{1}{2}yPe_b^{-1}) - \gamma_r(1-A)(1+\frac{1}{2}yPe_b^{-1})$, and we have neglected terms of $O(Pe_b^{-3})$. The quantities γ_i and e_i are projections of $\langle\hat{\boldsymbol{\Gamma}}\rangle\cdot\hat{\boldsymbol{r}}$ and $\langle\hat{\boldsymbol{E}}\rangle\cdot\hat{\boldsymbol{r}}$, respectively (cf. (B 2) and (B 3)), in the spherical coordinate system. Contrary to the full Smoluchowski equation, the diffusional terms in the left-hand side of (4.13) do not include a factor r^{-2}. Thus, this truncated equation overestimates diffusion at large radial separations. As a consequence, the growth of the wake region with increasing Pe_b is diminished; the wake, however, is still present and extends far downstream from the reference particle. This property makes this boundary-layer equation considerably simpler to solve numerically. In principle, the solution should be matched to a solution in the outer, convection-dominated region. This was not pursued because the matching will occur at different radial separations depending on the angles. Instead, the boundary-layer equation was taken to represent the solution

in the entire domain. The solution of the boundary-layer equation was obtained in the same way as that of the full Smoluchowski equation.

To extract results at large Pe_b for $b/a \to \infty$, for which there is a large accumulation of density in the boundary layer (cf. figure 9), a systematic dependence of the results on the angular resolution was noted. This problem was essentially eliminated by performing calculations as a function of angular resolution, followed by an extrapolation to infinite resolution.

5. Results

5.1. *Microstructure and rheology at small Pe*

It is well known that in the Smoluchowski equation at small Péclet numbers convection becomes as important as diffusion for sufficiently large separation distances $r \sim O(Pe^{-1/2})$. As a consequence, a regular perturbation expansion of the structure produces a solution that is valid to leading-order in an inner region which must be matched to the structure in the outer, convection-dominated region. This approach was adopted by Batchelor, who showed that the leading-order distortion of the structure is all that is required to calculate the zero-shear limiting viscosity of dilute Brownian hard spheres. To this order, the colloidal suspension is Newtonian as the normal stress differences are zero. Subsequently, Brady & Vicic (1995) demonstrated that the lowest-order term in the inner expansion for the structure that must be identified by matching to the outer solution is proportional to $Pe^{5/2}$. Consequently, the perturbation expansion of $f(\boldsymbol{r})$ proceeds as

$$f = f_1 Pe + f_2 Pe^2 + f_{5/2} Pe^{5/2} + \cdots \tag{5.1}$$

As the next higher-order term in the inner expansion is of $O(Pe^2)$, i.e. of lower order than the first mismatched term, it is sufficient to calculate this lower-order deformation of the structure to obtain the leading-order normal stress differences. It suffices also for determining the first correction to the equilibrium osmotic pressure, when the definition of this quantity is extended to finite Pe. The appearance of normal stresses at $O(Pe^2)$ signals the onset of non-Newtonian behaviour.

The approach adopted in this work is to solve the Smoluchowski equation by non-perturbative methods. Although higher-order terms in the perturbation expansion of the structure can be obtained, and have indeed already been discussed (Brady & Morris 1997; Vicic 1999), a matched asymptotic expansion approach rapidly becomes intractable as the Péclet number is increased further.

We will focus initially on the small-Pe departure from equilibrium as forced by a simple shear flow. The purpose of this is two-fold: first, the accuracy of the numerical solution method will be tested by comparing with the analytical and numerical results of the exact perturbation theory; secondly, higher-order corrections to the rheological properties of hard spheres will be determined, including the first correction to the Newtonian shear viscosity, which will remove any confusion caused by conflicting results reported in the past. To keep the number of parameters at a minimum, we restrict our attention initially to hard spheres, both in the presence and absence of hydrodynamic interactions. The effect of the extra excluded volume interactions is postponed for the moment until later sections.

Figure 3 shows calculated results for the structural distortion $f(\boldsymbol{r}) = g(\boldsymbol{r}) - 1$ in the absence of hydrodynamic interactions in the shear flow-gradient plane along the extensional axis – the $\theta = \frac{1}{4}\pi$ axis as measured from the axis extending in the

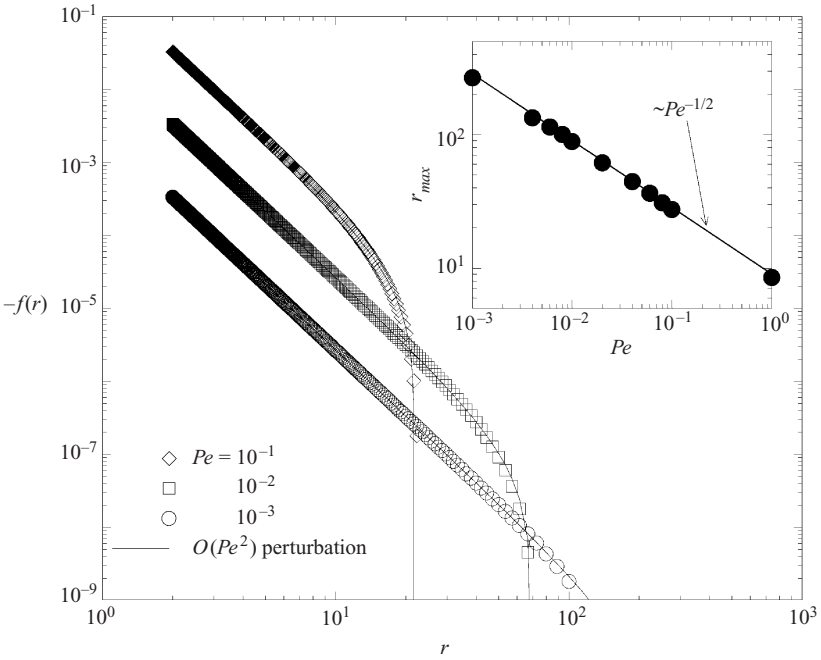

FIGURE 3. Structural deformation function $f(r)$ in the absence of hydrodynamic interactions as a function of radial separation r and Pe along the extensional axis in the shear flow-gradient plane. Solid lines show the analytical perturbation theory correct to $O(Pe^2)$. The inset illustrates that the separation distance where $f(r)$ is a maximum scales with $Pe^{-1/2}$.

direction of flow (see figure 2). For small separation distances the distortion decays as $-\frac{16}{3}r^{-3}Pe(\hat{\boldsymbol{r}}\hat{\boldsymbol{r}} : \hat{\boldsymbol{E}})$, as first determined by Batchelor (1977), which becomes $-\frac{8}{3}Pe$ on the extensional axis as seen in figure 3. Adding the $O(Pe^2)$ correction extends the range of validity of the solution to distances $rPe^{1/2} \sim O(1)$. As seen in figure 3, the inner solution correct to $O(Pe^2)$ describes the structure in a region that shrinks with increasing Pe. This behaviour is consistent with diffusion being increasingly confined to small separations, aside for regions in the flow where the relative particle velocity vanishes ($\theta \sim 0$ and π).

The $O(Pe^2)$ result is positive, and it enhances the particle density in the extensional quadrant such that $f(\boldsymbol{r})$ becomes positive at large separations. Sufficiently far from the reference particle, however, the structural distortion vanishes, which leads to a maximum in $f(\boldsymbol{r})$ on the extensional axis. The inset in figure 3 shows that the separation distance where $f(\boldsymbol{r})$ acquires a maximum value scales as $Pe^{-1/2}$, consistent with the rapid variation in $f(\boldsymbol{r})$ belonging to the matching region of the Smoluchowski equation. Previous workers have studied this region in detail via the Fourier transform of the structural distortion (Dhont 1989; Yan & Dhont 1993; Blawzdziewicz & Szamel 1993).

The rheological properties of hard-sphere suspensions in the absence of hydrodynamic interactions derive from the contact value of the pair-distribution function. In figure 4 this contact value is compared to the exact perturbation theory result in the shear flow-gradient plane ($\varphi = 0$). In this comparison, the $O(Pe^2)$ term has been isolated by showing $(f - f_1 Pe)/Pe$ as a function of Pe and comparing with the analytical result for $f_2 Pe = \frac{2}{27}Pe(\sin^2\theta - \cos^2\theta) + \frac{94}{945}Pe$. As seen, the f_2 term

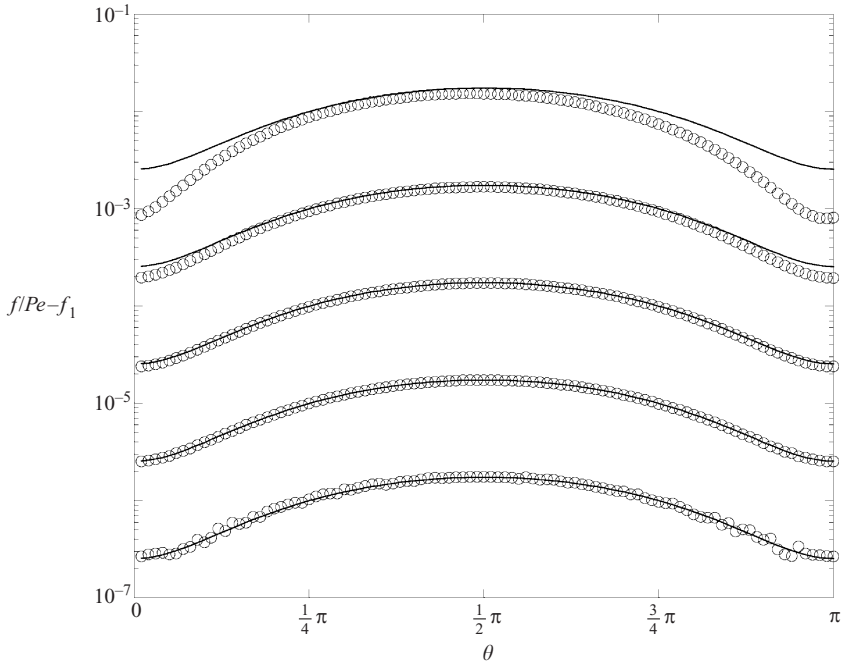

FIGURE 4. Angular dependence of $f(\boldsymbol{r})$ at contact ($r = 2$) in the shear flow-gradient plane as a function of the Péclet number in the absence of hydrodynamic interactions; from bottom-to-top: $Pe = 10^{-5}$, 10^{-4}, 10^{-3}, 10^{-2} and 10^{-1}. Solid lines show the analytical $O(Pe^2)$ perturbation result: $Pe\left(\frac{2}{27}(\sin^2\theta - \cos^2\theta) + \frac{94}{945}\right)$ (Brady & Vicic 1995).

captures the angular behaviour of the structural distortion up to $Pe \approx 0.01$. The next correction to this result is a depletion of particle density for all θ.

For hard spheres in the absence of hydrodynamic interactions, the result of the perturbation theory of Brady & Vicic is summarized by the following expression for the particle stress

$$\frac{\boldsymbol{\Sigma}_P}{\eta_s\dot{\gamma}\phi^2} = -\frac{nkT(1+4\phi)}{\eta_s\dot{\gamma}\phi^2}\boldsymbol{I} + \tfrac{24}{5}\langle\hat{\boldsymbol{E}}\rangle - Pe(\tfrac{16}{15}(\langle\hat{\boldsymbol{E}}\rangle\cdot\langle\hat{\boldsymbol{\Omega}}\rangle + \langle\hat{\boldsymbol{\Omega}}\rangle^T\cdot\langle\hat{\boldsymbol{E}}\rangle) + \tfrac{304}{105}\langle\hat{\boldsymbol{E}}\rangle:\langle\hat{\boldsymbol{E}}\rangle\boldsymbol{I} + \tfrac{32}{35}\langle\hat{\boldsymbol{E}}\rangle\cdot\langle\hat{\boldsymbol{E}}\rangle) + O(Pe^{3/2}). \quad (5.2)$$

From this equation it is an easy task to extract the Newtonian shear viscosity and the leading-order corrections to Newtonian rheological behaviour. The relative shear viscosity, which is defined as the shear stress normalized by $\eta_s\dot{\gamma}$, is identified as $\eta_r = 1 + \frac{5}{2}\phi + \frac{12}{5}\phi^2$, and the first and second normal stress differences are given by $N_1/\eta_s\dot{\gamma}\phi^2 = \frac{16}{15}Pe$ and $N_2/\eta_s\dot{\gamma}\phi^2 = -\frac{16}{21}Pe$. Finally, the shear-dependent osmotic pressure is obtained from the trace of the particle stress as $\Pi/nkT = 1 + 4\phi + \frac{16}{45}\phi Pe^2$. Analogous results for hard spheres with hydrodynamic interactions have been reported by Brady & Morris (1997).

The Newtonian shear viscosity for hydrodynamically interacting hard spheres (approximated by $b/a = 1.00001$) is calculated numerically as $\eta_r = 1 + \frac{5}{2}\phi + 5.92\phi^2$ in this work, which comprises the hydrodynamic high-frequency shear viscosity $\eta_r^H = 1 + \frac{5}{2}\phi + 5.00\phi^2$ summed with the Brownian contribution $\eta_r^B = 0.92\phi^2$. To identify the leading-order corrections to the ϕ^2–coefficients, we define the deviations: $\Delta\eta^{Total}/\phi^2 = 5.92 - (\eta_r - 1 - \frac{5}{2}\phi)/\phi^2$, $\Delta\eta^H/\phi^2 = (\eta_r^H - 1 - \frac{5}{2}\phi)/\phi^2 - 5.00$, and

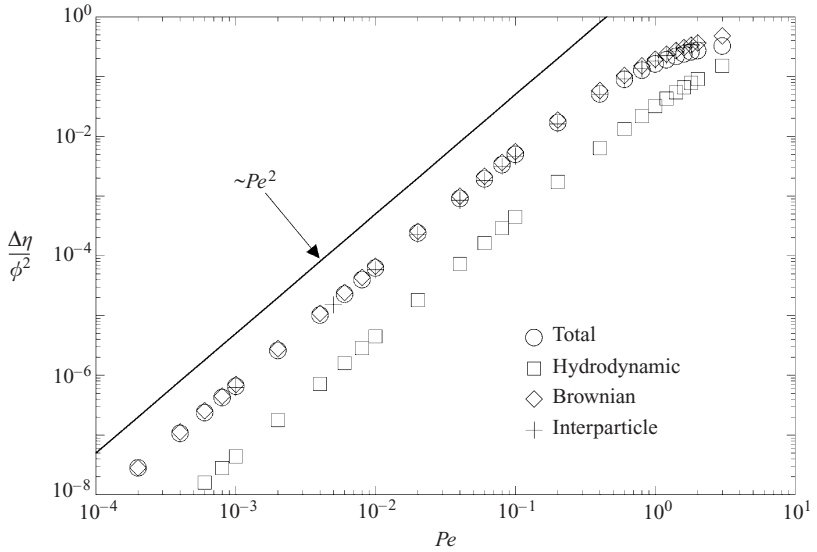

FIGURE 5. Small Pe variation of the relative viscosity for hard spheres with and without hydrodynamic interactions. The following contributions are shown: $\Delta\eta^{Total} = 5.92\phi^2 - (\eta_r - 1 - 2.5\phi)$; $\Delta\eta^H = (\eta_r^H - 1 - 2.5\phi) - 5.00\phi^2$; $\Delta\eta^B = 0.92\phi^2 - \eta_r^B$; $\Delta\eta^P = 2.4\phi^2 - \eta_r^P$. Note that η_r^P is the hard-sphere viscosity in the absence of hydrodynamic interactions.

$\Delta\eta^B/\phi^2 = 0.92 - \eta_r^B/\phi^2$. Similarly, for hard spheres with no hydrodynamic interactions we write the deviation from the interparticle viscosity as $\Delta\eta^P/\phi^2 = \frac{12}{5} - \eta_r^P/\phi^2$.

Figure 5 shows the deviations from the Newtonian viscosity as functions of Pe. All are positive, showing that the total viscosity decreases initially as Pe increases. The purely hydrodynamic component of the viscosity is found to increase monotonically with Pe, which agrees qualitatively with Stokesian dynamics simulations of concentrated systems (Foss & Brady 2000*b*). This result differs, however, from the Lionberger study, in which this contribution was found to exhibit a minimum at a Pe value slightly above unity. We can only conjecture that this discrepancy is connected to the different strategies used to enforce the far field boundary condition in the numerical solution for the microstructure (see § 4).

Both the hydrodynamic and Brownian contributions to the viscosity deviate from their Newtonian values with low Pe asymptotes proportional to Pe^2. This arises through the $O(Pe^3)$ perturbation to the structure, f_3, which produces a Brownian viscosity of $O(Pe^2)$. In contrast to the Brownian contribution, the hydrodynamic viscosity increases with Pe. However, at small Pe the variation in the hydrodynamic viscosity is more than an order of magnitude smaller than the variation in the Brownian component, so the net result is a shear thinning viscosity. The results in figure 5 are consistent with the analysis of Brady & Vicic (1995), in which they determined that $f_{5/2}$ only contributes to the isotropic stress. Previous studies predicted that the viscosity shear thins proportional to $Pe^{1/2}$ (Dhont 1989), but the influence of the no-flux boundary condition was neglected. It is the no-flux boundary condition that forces a finite structural deformation, and it acts as a quadrupole forcing, which ultimately sets the first mismatched term at $O(Pe^{5/2})$ in the expansion.

Figure 5 reveals unexpectedly that the hard-sphere viscosity of suspensions in the absence of hydrodynamic interactions shear thins in near quantitative agreement with the Brownian viscosity contribution of hard spheres with hydrodynamic interactions

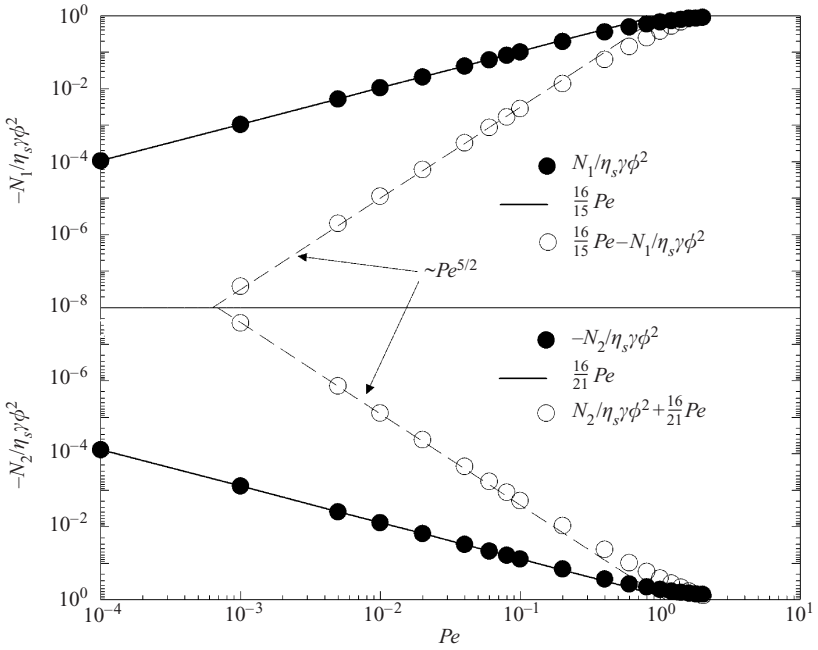

FIGURE 6. Small Pe variation of first and second normal stress differences for hard spheres without hydrodynamic interactions. Solid lines show exact results of the $O(Pe^2)$ perturbation theory.

included. Hence, at least for dilute suspensions, adding a static, high-frequency viscosity to the viscosity determined without hydrodynamics will produce an excellent approximation for $Pe < 1$. Thus, the absence of hydrodynamic interactions does not affect the fact that the viscosity decreases at small shear rates as Pe^2, despite what may be inferred from previous numerical results (Blawzdziewicz & Szamel 1993).

The present results confirm what has been known for some time: shear thinning is not caused by an ordering of the particles in the flow (Ackerson 1990); rather, it is caused by the decrease of the Brownian contribution to the viscosity, which far outweighs the small increase of the hydrodynamic component with Pe. Brownian motion tends to restore the equilibrium configuration, but, as the strength of the flow increases, the relative time scale available for the Brownian movement to achieve structural relaxation progressively decreases as directly reflected by the Péclet number; consequently, the Brownian contribution to the viscosity decreases. Computer simulations (Bossis & Brady 1989; Phung *et al.* 1996; Foss & Brady 2000*b*) and recent, detailed experimental measurements (Bender & Wagner 1995; Kaffashi *et al.* 1997; O'Brien & Mackay 2000) are all in firm agreement on this point.

As discussed in detail in past work (Brady & Vicic 1995; Brady & Morris 1997), asymmetries in the pair-distribution function result in finite normal stress differences. Figure 6 shows that the numerical solution based on the spherical harmonic expansion of the microstructure is able to reproduce the exact small-Pe limiting behaviour of the normal stress differences for hard spheres in the absence of hydrodynamic interactions. The normal stress differences are seen to be proportional to Pe^2 for small Pe, and they are caused by the second-order microstructure deformation f_2 in the regular perturbation expansion (5.1) (Brady & Vicic 1995). The first normal stress difference is positive at small Pe, whereas the second normal stress difference is negative.

By subtracting the exact small-Pe limits from the normal stress differences, we

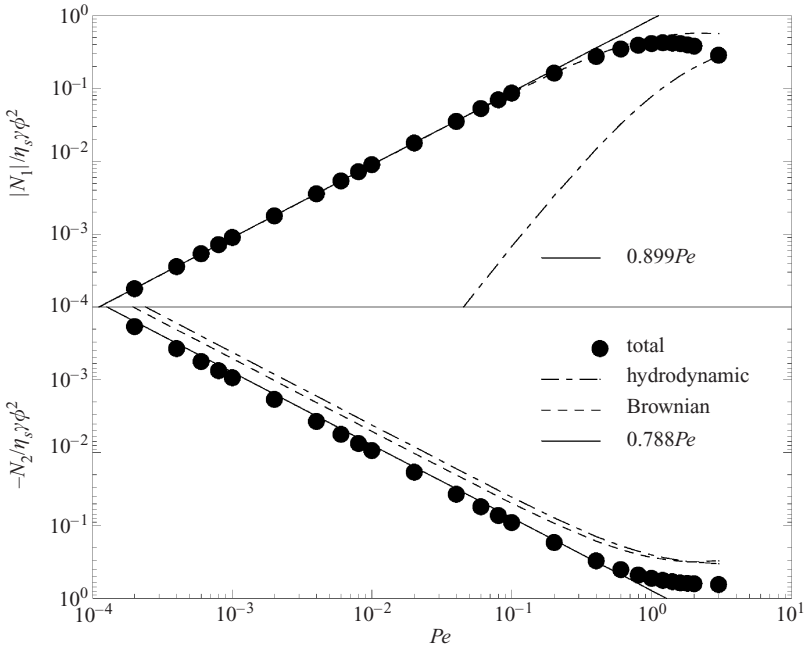

FIGURE 7. Small Pe variation of the first and second normal stress differences for hard spheres in the presence of hydrodynamic interactions. Note that the hydrodynamic contribution to N_1 is negative, as are all the contributions to N_2. Solid lines show exact results of the $O(Pe^2)$ perturbation theory for the (total) normal stresses: $N_1/\eta_s\dot{\gamma}\phi^2 = 0.899Pe$ and $N_2/\eta_s\dot{\gamma}\phi^2 = -0.788Pe$ (Brady & Vicic 1995). Our numerical results for the hydrodynamic and Brownian contributions are shown as broken curves.

find that the next higher-order contribution to both N_1 and N_2 is proportional to $Pe^{7/2}$. This observation is consistent with the matched asymptotic analysis of Brady & Vicic, who determined that $f_{5/2}$ in (5.1) only contributes to the osmotic pressure. Furthermore, Vicic (1999) has shown that – provided the expansion (5.1) proceeds in half-order powers of Pe – a f_3Pe^3 regular term in (5.1) only contributes to the shear viscosity and the osmotic pressure, but leaves the normal stress differences unchanged from their initial, small-Pe asymptotes. The results in figures 5 and 6 (cf. also figure 8) demonstrate that this is indeed the case.

Adding the effect of hydrodynamic interactions ($b/a = 1.00001$) does not alter the qualitative behaviour of the normal stress differences in the small Pe limit. As seen in figure 7, N_1 is positive and N_2 is negative, and both are proportional to Pe^2 in the limit $Pe \to 0$. Figure 7 further demonstrates that the positive Brownian contribution far outweighs the negative hydrodynamic contribution to N_1 (which is proportional to $Pe^{7/2}$), whereas the Brownian and hydrodynamic contributions to N_2 are both negative and of similar magnitude. Again, the numerical solution method is in good agreement with the exact small-Pe asymptotic results of Brady & Vicic, which give $N_1 = 0.899\eta_s\dot{\gamma}\phi^2 Pe$ and $N_2 = -0.788\eta_s\dot{\gamma}\phi^2 Pe$ for $Pe \to 0$. Although not shown in figure 7, the next higher-order contributions to N_1 and N_2 are proportional to $Pe^{7/2}$, as for hard spheres without hydrodynamic interactions.

Shear-induced anisotropies in the microstructure lead to departures in the generalized, shear-dependent osmotic pressure from its equilibrium value. Note that the osmotic pressure of hard spheres without hydrodynamics is of a particularly simple form (see (3.8)), and reflects only changes in the contact value of the pair-distribution

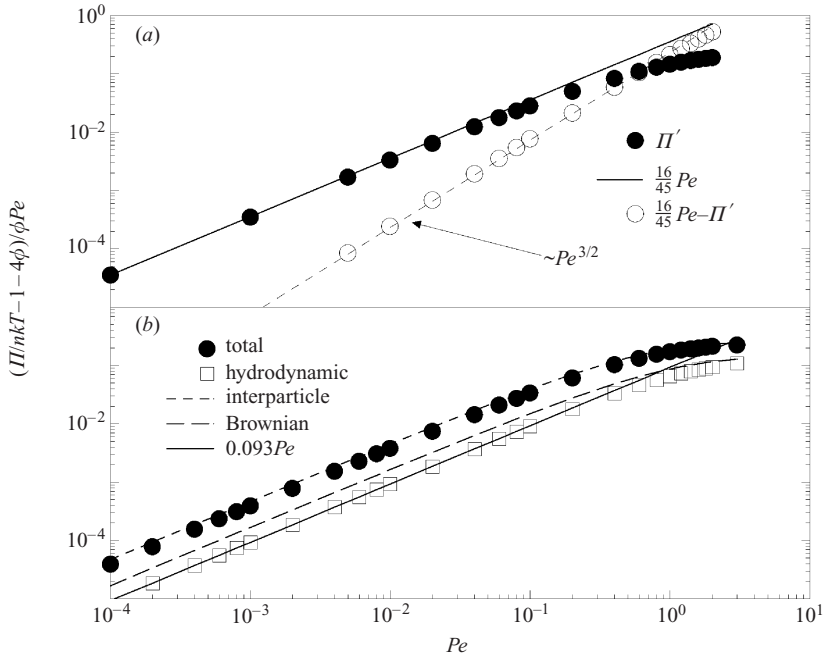

FIGURE 8. Small Pe variation of the generalized, shear-dependent osmotic pressure for hard spheres (a) without hydrodynamic interactions, and (b) with hydrodynamics. In (a) $\Pi' = (\Pi/nkT - 1 - 4\phi)/\phi Pe$. A least-squares fit yields $\Pi' = 0.374Pe$ for hard spheres with hydrodynamics. In (b) the Brownian contribution is negative, and the solid line shows the exact result for the hydrodynamic contribution: $\Pi'^H = 0.093Pe$ (Jeffrey *et al.* 1993). Note that the hard-sphere limit is approximated by a small excluded volume parameter, $b/a - 1 = 10^{-5}$, which explains the presence of an interparticle contribution to the osmotic pressure.

function. Brady & Vicic determined that the initial departure from the equilibrium value of the osmotic pressure is caused by the $f_2 Pe^2$ term in (5.1). The numerical results in figure 8 are in accord with this conclusion. Figure 8(a) shows that the osmotic pressure of hard spheres in the absence of hydrodynamic interactions is increased over its equilibrium value by a weak flow. The next higher-order contribution to the osmotic pressure originates from $f_{5/2} Pe^{5/2}$ in (5.1), which is the first mismatched term between the inner and outer expansions of the microstructure. This finding is in agreement with the matched asymptotic analysis of Brady & Vicic, who found this term to contribute only to the osmotic pressure while leaving the other viscometric functions unchanged.

For hard spheres with hydrodynamic interactions ($b/a = 1.00001$) the osmotic pressure is determined by several contributions, all of which are proportional to Pe^2 at small Pe. Figure 8(b) shows that the purely hydrodynamic contribution is positive, and it shows that the numerical results compare well with the leading-order deviation calculated by Jeffrey *et al.* (1993). The contribution which is labelled as Brownian in this figure derives from the Brownian stress quoted in (3.7) and is negative. It is an indirect hydrodynamic contribution as it involves one of the pressure moments defined by Jeffrey *et al.* (1993) (see also Appendix B), as well as radial density gradients. Because we do not treat the exact hard-sphere limit – having instead approximated hard spheres by a small value of the excluded volume parameter, specifically $b/a - 1 = 10^{-5}$ – the usual hard-sphere contact contribution

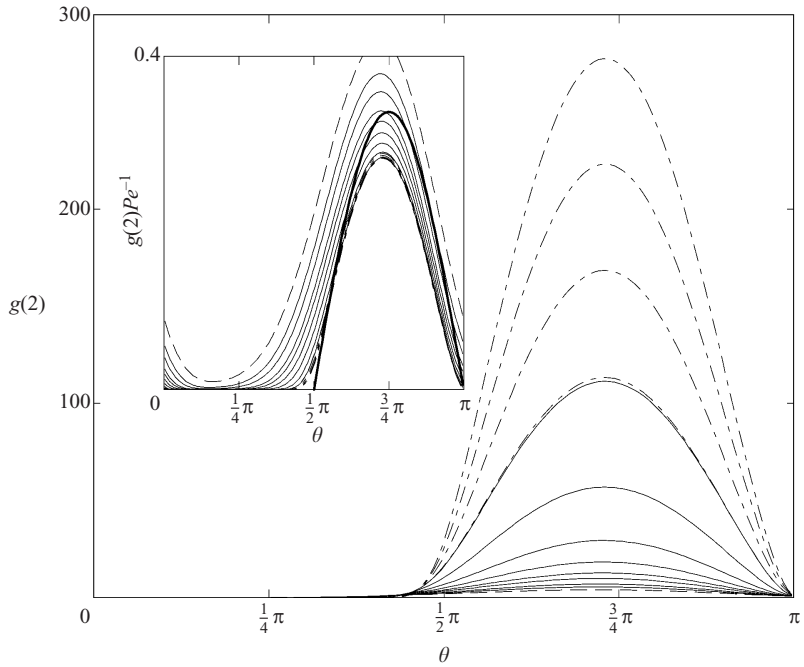

FIGURE 9. The non-equilibrium pair-distribution function at contact in the shear flow-gradient plane as a function of θ and Pe for hard spheres in the absence of hydrodynamic interactions. Results from the solution of the full Smoluchowski equation are shown as solid lines and the solutions from the boundary-layer equation are shown as dashed curves. From bottom-to-top: $Pe = 10$ (dashed line), 15, 20, 30, 40, 60, 100, 200 and 400; and from the boundary-layer equation $Pe = 400$, 600, 800 and 1000. The inset shows the same results scaled by Pe; here, the bold curve is the $Pe \to \infty$ prediction from the boundary-layer theory of Brady & Morris (1997): $g(2,\theta,0)Pe^{-1} = -\frac{2}{3}\sin\theta\cos\theta$.

belongs by definition to the interparticle stress. This explains the appearance of an interparticle contribution to the hard-sphere osmotic pressure. For true hard spheres, this contribution would be labelled as Brownian, and it would be indistinguishable from the interparticle contribution in figure 8.

5.2. *Microstructure and rheology at large Pe*

As described in §4, the direct numerical solution of the surface spherical harmonic expansion of the Smoluchowski equation becomes too expensive computationally at $O(1)$ values of Pe. Applying the finite-difference scheme to the Smoluchowski equation extends the numerical solution to $Pe \approx 200$. For even higher Pe, a simpler equation is solved that is valid near $r = 2$ where the boundary-layer appears in the compressional quadrant of the flow. This boundary-layer equation is derived in Appendix B.

For hard spheres in the absence of hydrodynamic interactions there is no reduction of the mobility when two particles approach one another. As a consequence, particle density in the boundary-layer accumulates rapidly with increasing Pe. The reference particle acts as an obstruction to particles being advected from upstream, and they are collected in a small region near particle contact in the compressional quadrant of the flow ($\frac{1}{2}\pi < \theta < \pi$). Downstream from the reference particle, in the extensional region of the flow, there is no obstruction to transport, and particles are simply advected downstream and the boundary-layer does not exist in this region (cf. figure 1). For strong flows, large density gradients develop in the boundary-layer such that there is

a significant driving force for diffusion at small particle separations despite the strong convection forces.

Figure 9 shows the contact value of the non-equilibrium pair-distribution function $g(\boldsymbol{r})$ in the shear flow-gradient plane ($\varphi = 0$) as a function of the angle θ and Pe for hard spheres under neglect of hydrodynamic interactions. As seen, there is a build-up of particle density in the compressional region with increasing Pe, whereas the extensional region is almost entirely depleted of particles at large Pe. The inset demonstrates that the growth of the boundary-layer scales linearly with Pe. Moreover, the density profiles collapse onto a single curve at high Pe when scaled by Pe. This result is consistent with the boundary-layer theory of Brady & Morris (1997), although the shape and precise growth rate with Pe differ somewhat. They obtained the following approximate result for the pair-distribution function at contact in the compressional region as $Pe \to \infty$

$$g(2) = -\tfrac{2}{3} Pe \sin\theta \cos\theta \cos\varphi. \tag{5.3}$$

This result is shown in the inset of figure 9 as the bold curve. The maximum value of $g(2)$ is located on the compressional axis ($\theta = \frac{3}{4}\pi$), whereas the actual maximum occurs slightly further downstream. In addition, the pair-distribution function is more attenuated than the theoretical prediction. The maximum of $g(2)$ is pushed downstream because of vorticity, an effect that will be seen to be far more pronounced when hydrodynamic interactions are not neglected (cf. figure 10), whereas the broadening of $g(2)$ is caused by angular diffusion. Both vorticity and angular diffusion were neglected in the asymptotic theory of Brady & Morris; in particular, they restricted diffusion to the radial direction, which removes a mode of escape from the boundary layer and causes an overestimation of $g(2)$. Nevertheless, the important facts that the contact value of the pair-distribution function grows linearly with Pe and that the boundary layer is absent downstream from the reference particle are correctly captured by their theory. These slight deviations affect the numerical values for the rheological properties as $Pe \to \infty$, particularly N_1.

There are two curves shown for $Pe = 400$ in figure 9, one resulting from the solution of the full Smoluchowski equation, and the other resulting from the solution of the boundary-layer equation. The two solutions are in close agreement, which demonstrates that the simpler boundary-layer equation provides an accurate description of the boundary-layer structure.

The inclusion of hydrodynamic interactions does not significantly alter the characteristic features of the boundary layer. The results for near hard spheres ($b/a = 1.00001$) in figure 10 show that the particle density increases with increasing Pe in the compressional region of the flow, while the extensional region becomes progressively more depleted. However, the detailed structure of the boundary-layer differs from the case of hard spheres in the absence of hydrodynamic interactions. The magnitude of the pair-distribution function at contact is markedly smaller for a given Pe. Also, with increasing Pe, the angular location of the maximum is displaced downstream from the compressional axis. Both of these effects are explained by the presence of hydrodynamic lubrication forces. Just as the squeezing together of two particles in the compressional region of the flow is resisted by the expulsion of solvent from the narrow gap separating them, so is the pulling apart of the pair in the extensional region resisted by the replenishment of solvent in the growing gap. The former action tends to decrease the contact density in the compressional region, and the latter action creates a finite contact density in the extensional region.

The Pe-dependence of the angular location of the maximum value of $g(2)$ is

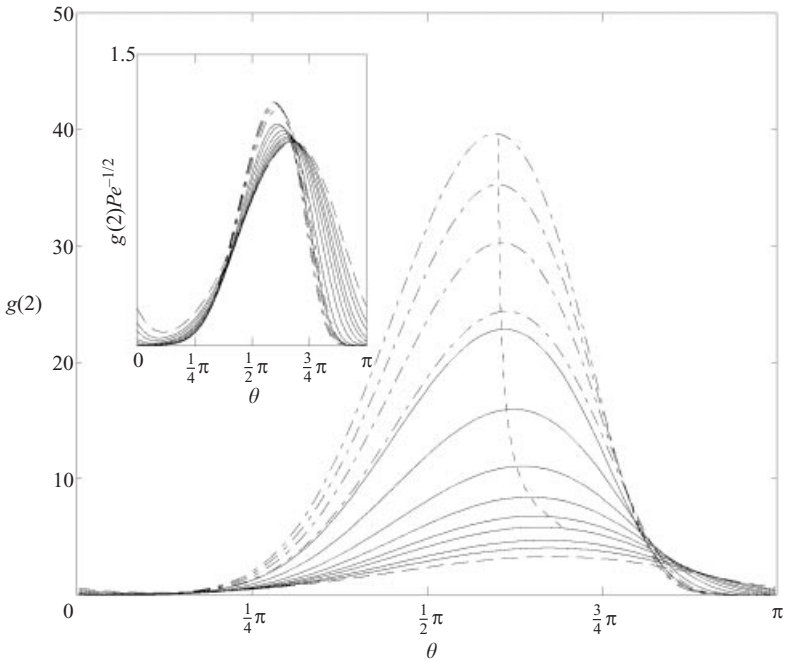

FIGURE 10. The non-equilibrium pair-distribution function at contact in the shear flow-gradient plane as a function of θ and Pe for hard spheres with hydrodynamics ($b/a = 1.00001$). Results from the solution of the full Smoluchowski equation are shown as solid lines and the solutions from the boundary-layer equation are shown as dashed curves. From bottom-to-top: $Pe = 10$ (dashed line), 15, 20, 30, 40, 60, 100, 200 and 400 (bold line); and from the boundary-layer equation $Pe = 400$, 600, 800 and 1000. The short-dashed curve is a best fit to the maxima in $g(2)$. The inset shows that scaling by $Pe^{1/2}$ reduces the maximum in the compressional quadrant to $O(1)$.

described by $0.60\pi + O(Pe^{-1})$, which suggests that the particle density in the boundary-layer is distributed asymmetrically even on approaching the $Pe^{-1} = 0$ limit. The inset in figure 10 shows that the contact value of the pair-distribution function no longer scales linearly with Pe as in the absence of hydrodynamic interactions. Instead, a sublinear scaling in the neighbourhood of $Pe^{1/2}$ is evidently followed. Brady & Morris determined an increase proportional to $Pe^{0.78}$ for true hard spheres in pure straining flow. The exponent 0.78 comes from matching with the outer, non-Brownian solution of Batchelor & Green (1972), which is strictly valid only for pure straining motion. The presence of closed particle trajectories in the $Pe^{-1} = 0$ limit in simple shear flow precludes a determination of the outer solution and the exponent may differ from 0.78. Preliminary results for near hard spheres in planar extensional flows suggest indeed that the contact value of $g(\boldsymbol{r})$ on the compressive axes scales as $Pe^{0.78}$.

This weaker accumulation of particle density in the boundary layer is compensated by a concomitant increase of the boundary-layer thickness, which is found to scale close to $Pe^{-1/2}$, such that a volume integration over the pair-distribution function in the boundary-layer may yield a finite result in the $Pe^{-1} \to 0$ limit. However, the analysis of Brady & Morris demonstrates that hydrodynamically interacting hard spheres at $Pe^{-1} = 0$ is a special case within this singular limit for which we should expect a disparity in the Pe-scalings of the boundary-layer density (less than Pe) and thickness (Pe^{-1}) such that non-Newtonian effects vanish irrespective of the boundary-layer asymmetry. We see that even an excluded volume parameter $b/a = 1.00001$

differs from the pure-hydrodynamic limit and results in non-zero non-Newtonian effects as $Pe \to \infty$. The magnitude of the non-Newtonian effects, particularly the normal stress differences, however, are found to extrapolate to values close to zero as $b/a \to 1$, in keeping with the analysis of Brady & Morris. This observation is also in agreement with the calculations of Zarraga & Leighton (2001) and Wilson & Davis (2000), both of whom considered the non-Brownian, $Pe^{-1} = 0$ limit.

5.3. *Effect of excluded volume repulsion*

To study the effect of repulsive interactions on the rheology, we employ the simple excluded volume interaction in (2.5), whereby particles are maintained at least a distance $2b > 2a$ from one another. Thus, in addition to the volume fraction and the Péclet number, the parameter b/a is introduced which characterizes the range of the repulsive interaction. The cases discussed so far, hydrodynamically interacting near hard spheres and hard spheres in the absence of hydrodynamic interactions, correspond to the two limits $b/a = 1.00001 \approx 1$ and $b/a \to \infty$, respectively. By selecting b/a values intermediate to these limits, we tune the interactions in the suspension from being hydrodynamically dominated at b/a values near unity to purely thermodynamic in the $b/a \to \infty$ limit.

Figure 11 shows the variation of the ϕ_b^2-coefficient of the shear viscosity with Pe_b, where $\phi_b = (b/a)^3 \phi$ and $Pe_b = (b/a)^2 Pe$. The shear viscosity has been divided into contributions resulting from hydrodynamic interactions, Brownian motion, and interparticle force interactions, the sum of which yields the total shear viscosity. This division of the shear viscosity corresponds to the division of the particle stress in (3.6)–(3.8). For b/a values close to unity ($b/a = 1.00001$ and 1.001), where hydrodynamic interactions are important, the shear viscosity first shear thins and then shear thickens. At small Pe_b, the shear viscosity is Newtonian and is determined essentially by a hydrodynamic contribution and a smaller, but significant, Brownian contribution. At intermediate Pe_b the viscosity shear thins, which is caused by the decrease of the Brownian contribution. As Pe_b is further increased, the Brownian contribution becomes negligible, and the shear viscosity is determined essentially only by the hydrodynamic component. Since the hydrodynamic viscosity is a monotonically increasing function of Pe_b as particles are driven into close lubrication contact by the shearing forces, the viscosity shear thickens. This behaviour is completely in accord with Stokesian dynamics simulations (Phung *et al.* 1996; Foss & Brady 2000*b*).

On increasing b/a further, the ϕ_b^2-coefficient in the viscosity expansion decreases. This behaviour is, however, somewhat deceiving because of the normalization chosen. Extracting instead the coefficient in front of ϕ^2 – the volume fraction based on the actual, physical size of the particles – the results in figure 11 must be multiplied by $(b/a)^6$. The results now show that the Newtonian low-shear viscosity increases as b/a increases. In fact, hard spheres with $b \equiv a$ yield the smallest low-shear viscosity, in agreement with the notion that both repulsive and attractive (see, however, Bergenholtz & Wagner 1994) interactions increase the low-shear viscosity over that of hard-sphere suspensions (Russel 1984; Russel *et al.* 1989).

When the range of the repulsion is increased, particle pairs no longer experience the full extent of the lubrication forces, which only act close to physical particle contact. As a consequence, an overall lower total shear viscosity to $O(\phi_b^2)$ is obtained, but one which has significant contributions from all sources of interactions. For $b/a = 1.1$, the interparticle contribution is the dominant thermodynamic contribution. Recalling that effects of Brownian motion only appear indirectly through hydrodynamic coupling, we can rationalize the overall decrease of the Brownian contributions with increasing

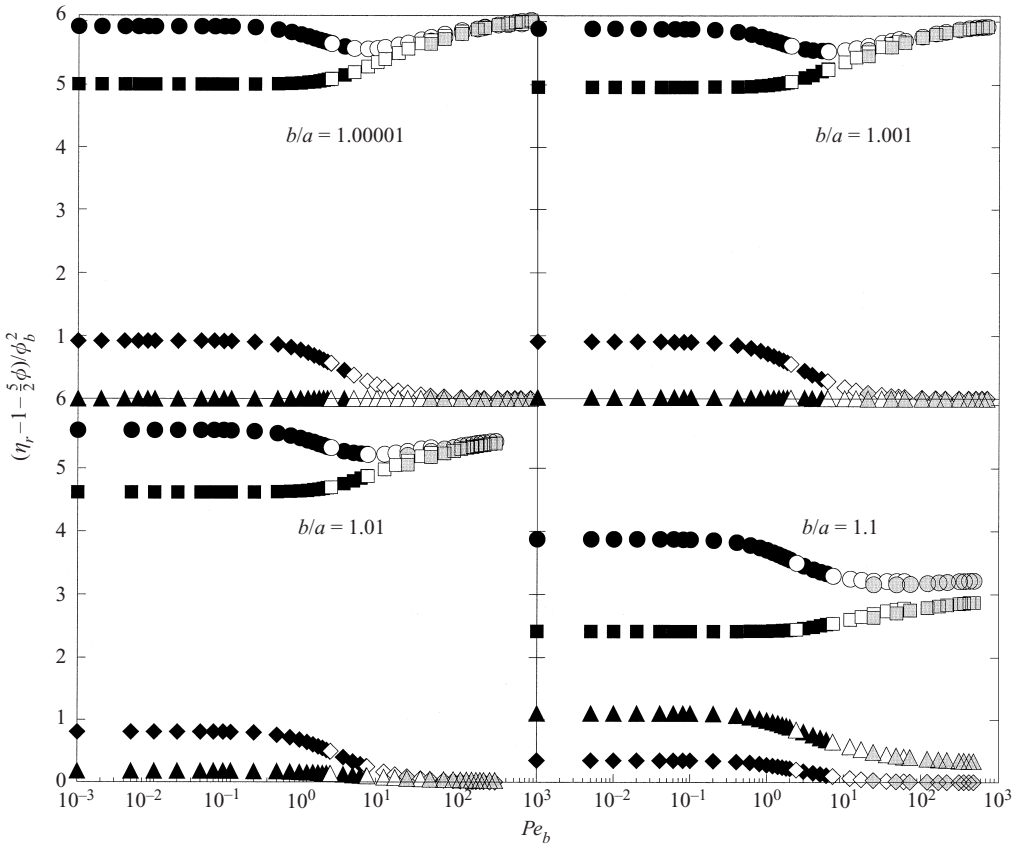

FIGURE 11. Contributions to the ϕ_b^2-viscosity coefficient as functions of Pe_b and b/a: ○, total; □, hydrodynamic; ◇, Brownian; △, interparticle force contribution to the viscosity. The numerical solution method is indicated by the pattern: filled, surface spherical harmonic expansion; unfilled, finite-difference solution; tinted, finite-difference solution of the boundary-layer equation.

b/a since hydrodynamic interactions become weaker with increasing b/a. This is also evident from the smaller, though still dominant, hydrodynamic viscosity for $b/a = 1.1$. At large Pe_b, the weak shear thickening of the hydrodynamic viscosity is counterbalanced by the shear thinning of the interparticle viscosity such that a nearly Newtonian high-shear viscosity results. Hence, $b/a \approx 1.1$ delineates suspensions for which the viscosity shear thins followed by some amount of shear thickening ($b/a < 1.1$) and those which exhibit a shear thinning viscosity followed by a well-defined high-shear Newtonian plateau with no shear thickening ($b/a > 1.1$).

In the limit $b/a \to \infty$, corresponding to hard spheres under neglect of hydrodynamic interactions, the shear viscosity shown in figure 12 is determined by the interaction potential alone. The Newtonian low-shear plateau, where the ϕ^2-coefficient is equal to $\frac{12}{5}$, is followed by shear thinning, the initial part of which has been the focus of previous investigations (Blawzdziewicz & Szamel 1993; Lionberger 1998). At larger Pe, the viscosity reaches a terminal plateau with a ϕ^2-coefficient value not too much below unity. The boundary-layer analysis of Brady & Morris (1997) with the simple radial-balance approximation gives a somewhat higher prediction of $\frac{6}{5}$. Recalling that the shear viscosity in this limit is directly related to the contact value of the

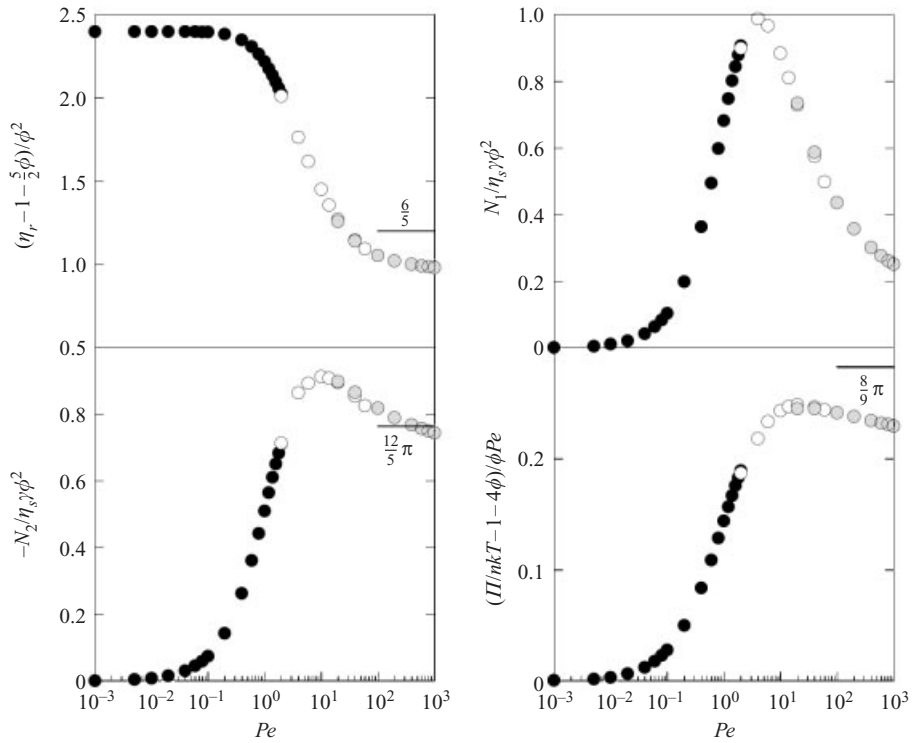

FIGURE 12. The ϕ^2-coefficients of the shear viscosity, first and second normal stress differences, and the osmotic pressure for hard spheres in the absence of hydrodynamic interactions as a function of Pe.

pair-distribution function, the source of the discrepancy is seen in figure 9 to be the overestimation of the density in the boundary-layer.

The ϕ_b^2-coefficient of the first normal stress difference is shown in figure 13 as a function of Pe_b and b/a. At small Pe_b, N_1 vanishes regardless of the b/a value, indicating indeed that the suspension behaves as a Newtonian liquid. As Pe_b is increased, the ϕ_b^2-coefficient of N_1 is initially positive, but changes sign as Pe_b is increased further. This trend holds for all b/a shown in figure 13. The main difference in going from small to larger b/a is a gradual shift from Brownian motion being the dominant thermodynamic contribution to N_1 for $b/a \approx 1$ to the interparticle force contribution exceeding the Brownian at $b/a = 1.1$.

For all Pe_b and b/a in figure 13 the hydrodynamic contribution to the ϕ_b^2-coefficient of N_1 is negative whereas the Brownian and interparticle force contributions are positive. The thermodynamic contributions to N_1 are proportional to the surface integral $-\int \mathrm{d}\Omega(\hat{z}\hat{z} - \hat{x}\hat{x})g(\Omega)$, which, with the coordinate system as in figure 2, becomes $-\int \mathrm{d}\varphi\,\mathrm{d}\theta \sin\theta(\cos^2\theta - \sin^2\theta\cos^2\varphi)g(\theta,\varphi) \sim -\int \mathrm{d}\theta \sin\theta\cos 2\theta g(\theta,0)$, where $\mathrm{d}\Omega = \mathrm{d}\varphi\,\mathrm{d}\theta\sin\theta$ is the solid angle. Since $\int_0^{2\pi} \mathrm{d}\varphi g(\theta,\varphi) \geqslant 0$ and $\int_0^{2\pi} \mathrm{d}\varphi\cos^2\varphi g(\theta,\varphi) \geqslant 0$, we have evaluated the expression in the shear plane $\varphi = 0$. With $g(\theta,0)$ from figures 9 and 10, we see clearly that the asymmetry about the compressive axis and the spill-over of probability density onto the extensional axis ($\frac{1}{4}\pi < \theta < \frac{1}{2}\pi$), most noticeable with hydrodynamics (figure 10), generates a positive thermodynamic N_1.

Determination of the sign of the hydrodynamic contribution to N_1 requires a more careful consideration of the fore–aft asymmetry within the boundary

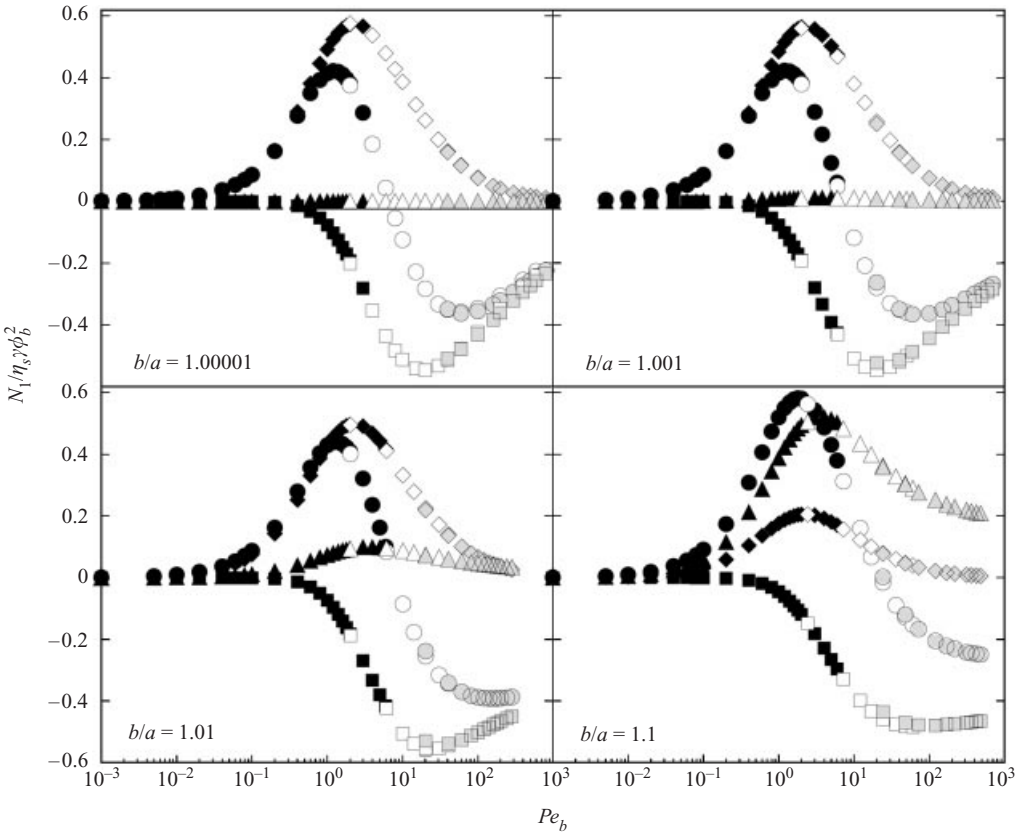

FIGURE 13. Contributions to the ϕ_b^2-coefficient of the first normal stress difference as functions of Pe_b and b/a. Legend as in figure 11.

layer. The dominant contribution comes from near-touching particles and we can estimate the stress from the force moment $-\langle \boldsymbol{r}\boldsymbol{F}^H_{lub}\rangle$, with the hydrodynamic lubrication force $\boldsymbol{F}^H_{lub} \approx -6\pi\eta_s a^2 \hat{\boldsymbol{r}}(\hat{\boldsymbol{r}} \cdot \langle \hat{\boldsymbol{E}} \rangle \cdot \hat{\boldsymbol{r}})$. Hence, we expect the hydrodynamic stress to behave as $\int \mathrm{d}\Omega \hat{\boldsymbol{r}}\hat{\boldsymbol{r}}(\hat{\boldsymbol{r}} \cdot \langle \hat{\boldsymbol{E}} \rangle \cdot \hat{\boldsymbol{r}}) g(\Omega)$. The hydrodynamic contribution to N_1 follows as $N_1^H \sim \int \mathrm{d}\varphi \, \mathrm{d}\theta \sin^2\theta \cos\theta (\cos^2\theta - \sin^2\theta \cos^2\varphi) g(\theta, \varphi)$. Again, we evaluate the pair-distribution function in the shear plane ($\varphi = 0$), which gives $N_1^H \sim \int \mathrm{d}\theta \sin^2\theta \cos\theta \cos 2\theta g(\theta, 0)$.

This analysis is too naive, however, because it neglects the internal structure of the boundary layer; it results in $N_1^H > 0$ when we use the pair-distribution function at $r = 2$ in figure 14. In contrast to the thermodynamic contributions to N_1, which are determined mainly by the angular location of the boundary layer in the shear plane, N_1^H is primarily determined by the angular asymmetry within the boundary layer. We must treat the boundary layer as having a finite radial thickness. Accordingly, we interpret $g(\theta, 0)$ in the simple analysis above as $\int_{bl} \mathrm{d}r g(r, \theta, 0)$ (or, more accurately, as $g(\theta, 0) \sim \int_{bl} \mathrm{d}r \, r^2 M(r) g(r, \theta, 0)$), where $\int_{bl} \mathrm{d}r \ldots$ denotes a radial integration over the extent of the boundary layer. From figure 14, in which the angular and radial dependence of the pair-distribution function in the boundary layer is shown for $b/a = 1.00001$ and $Pe = 200$, we observe that the boundary layer is convected downstream rapidly as the radial separation increases. Physically, particles must be

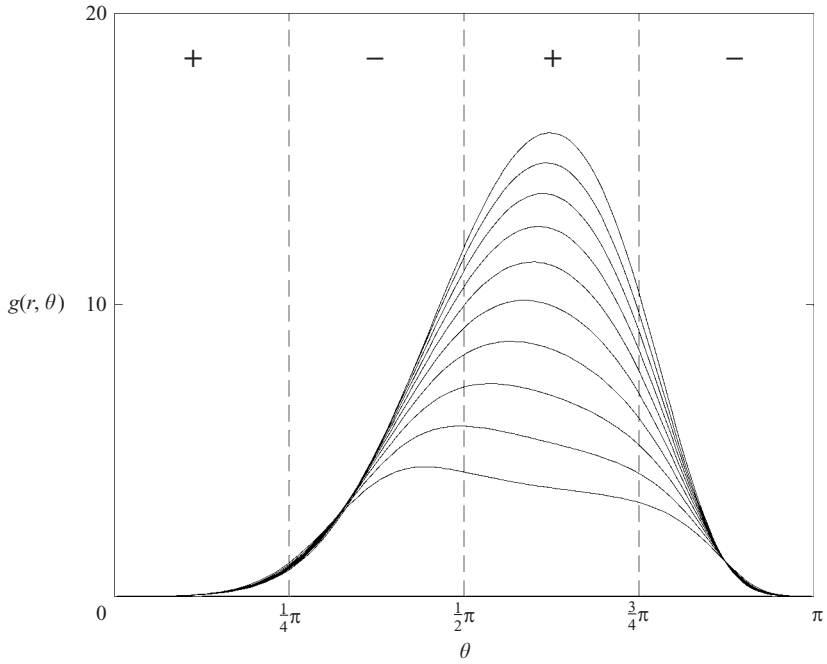

FIGURE 14. The non-equilibrium pair-distribution function for $b/a = 1.00001$ and $Pe = 200$ in the flow-gradient plane ($\varphi = 0$) as a function of the angle θ and interparticle separation. Shown from top-to-bottom are the separation distances $r = 2.0000$, 2.0007, 2.0014, 2.0023, 2.0034, 2.0049, 2.0069, 2.0098, 2.0144 and 2.0227. The signs denote regions where $\sin^2\theta\cos\theta\cos 2\theta$ assumes positive and negative values.

pulled apart on the extensional side to overcome the hydrodynamic lubrication forces, which results in the rheometer plates being pulled inward – a negative N_1.

In the absence of hydrodynamic interactions, or for $b/a \to \infty$, only the interparticle interactions determine N_1. For this case the ϕ^2-coefficient of N_1 is positive for all Pe, and, as shown in figure 12, it asymptotes to what appears to be a small positive value. The asymptotic boundary-layer calculation of Brady & Morris (1997) assumed symmetry about the compressive axis (in order to obtain an analytical solution) and therefore gives $N_1 = 0$ as $Pe \to \infty$ for dilute hard-sphere suspensions. The numerical solution reveals a small degree of asymmetry evident in figure 9 and therefore a finite N_1.

The ϕ_b^2-coefficient of the second normal stress difference is seen in figure 15 to be negative for all b/a and Pe_b, as are all its constituent contributions. In going from $b/a \approx 1$ to $b/a = 1.1$, the Brownian contribution decreases and is gradually overtaken by the interparticle force contribution, while the hydrodynamic contribution is seen to weaken. For large Pe_b, although difficult to ascertain from the results in figure 15, the ϕ_b^2-coefficient of N_2 appears to reach finite values that increase in magnitude as b/a is increased. This trend is in qualitative agreement with the results of Zarraga & Leighton (2001) and Wilson & Davis (2000) for non-Brownian spheres with the same excluded volume interaction as in (2.5).

Without any hydrodynamic interaction, the ϕ^2-coefficient of N_2, shown in figure 12, remains negative and asymptotes to a $Pe \to \infty$ value that is close to the theoretical prediction of Brady & Morris (1997) given by $12/(5\pi)$. The influence of the downstream wake, which is a source of microstructural asymmetry (see figure 1), is seen to

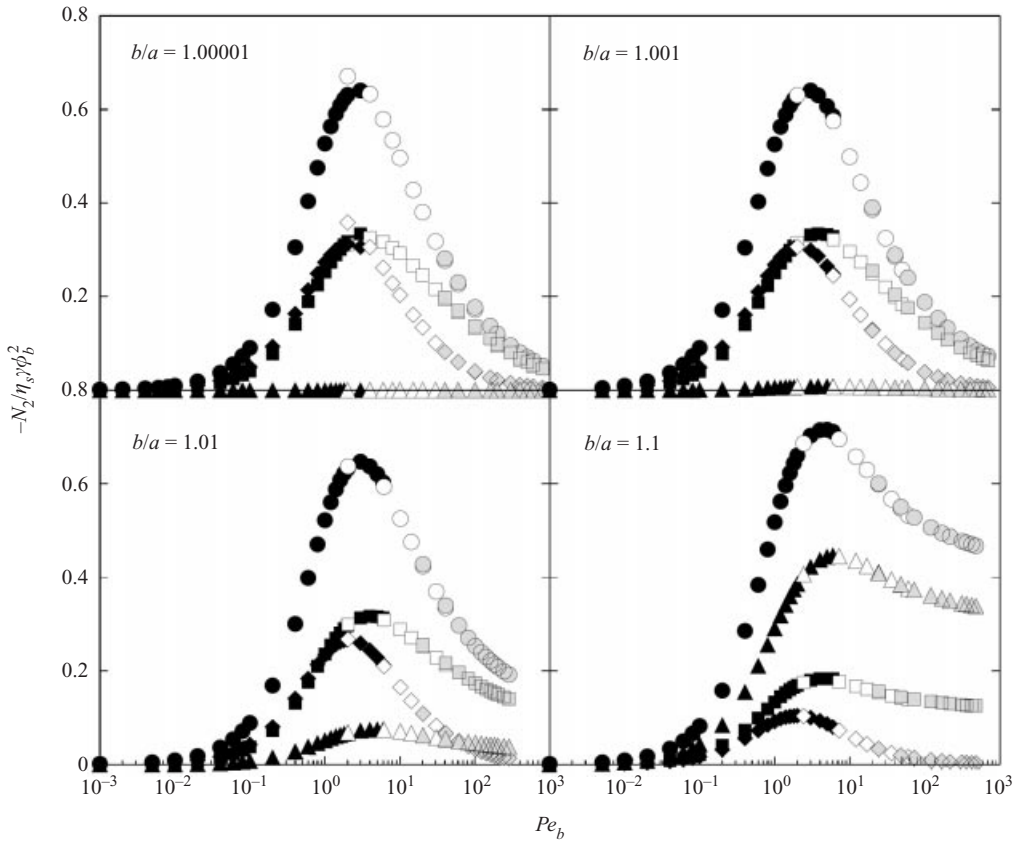

FIGURE 15. Contributions to the ϕ_b^2-coefficient of the second normal stress difference as functions of Pe_b and b/a. Legend as in figure 11.

be minor so far as N_2 is concerned, as the entire extensional quadrant was deleted in the Brady & Morris treatment. It suffices to account for the boundary-layer structure to obtain an accurate prediction for the $Pe \to \infty$ value of N_2 for dilute hard spheres. The calculations of Zarraga & Leighton (2001) for non-Brownian hard spheres also yielded a result consistent with that of the Brady & Morris prediction.

The pressure and isothermal compressibility of a system of rigid particles suspended in an incompressible solvent are indeterminate. Nevertheless, the colloidal particles are free to explore any configuration and the system exhibits a well-defined compressibility with respect to the particle coordinates. The suspension pressure in this sense is called the osmotic pressure. At equilibrium, the solvent degrees of freedom only appear indirectly through the particle–particle interaction potential (potential of mean force) $V(r)$. When the suspension is subjected to a flow the situation is no longer so simple. The solvent now contributes to the osmotic pressure both through the altered microstructure and through hydrodynamic interactions; the former is contained in $g(\boldsymbol{r})$ and the latter we have partitioned in hydrodynamic and Brownian parts in (3.6) and (3.7).

The osmotic pressure is shown as a function of Pe_b and b/a in figure 16. For $b/a < 1.1$, there is little difference among the results. A maximum is reached at $O(1)$ values of Pe_b. The maximum is caused by the interparticle component, since the hydrodynamic and Brownian contributions behave almost identically to one another

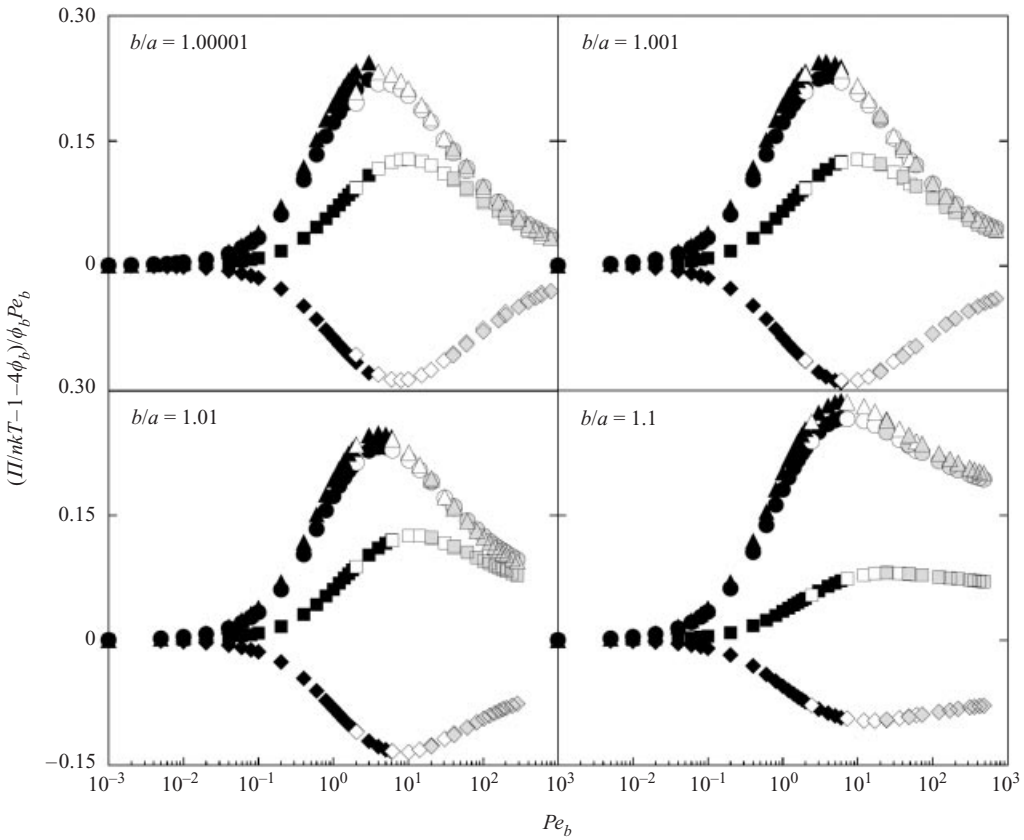

FIGURE 16. Contributions to the ϕ_b^2-coefficient of the osmotic pressure as functions of Pe_b and b/a. Legend as in figure 11.

but differ in sign. As seen in figure 16, this trend is independent of b/a. The sum of the hydrodynamic and Brownian contributions does not precisely vanish, however, which is demonstrated by the behaviour at small Pe in figure 8.

The large Pe limit is near zero for b/a of $O(1)$, which is caused by the sublinear increase in the accumulation of particle density in the boundary-layer. Upon increasing b/a, the hydrodynamic and Brownian contributions gradually decrease in magnitude, but the large Pe value increases in qualitative accord with the calculations of Zarraga & Leighton (2001). For hard spheres without hydrodynamic interactions, figure 12 shows that the limiting value $8/(9\pi)$, predicted by Brady & Morris (1997), gives a fairly accurate estimate for the $Pe^{-1} = 0$ limit of the osmotic pressure.

6. Discussion

The results of the previous sections illustrate, as noted by Russel (1980), that dilute colloidal suspensions possess the same characteristic non-Newtonian flow behaviour as concentrated suspensions. At small Péclet numbers, the shear viscosity exhibits a Newtonian plateau followed by shear thinning. At larger Péclet numbers, the shear thinning terminates either in a second Newtonian plateau or exhibits some degree of continuous shear thickening. The shear thinning is caused by a mechanism that

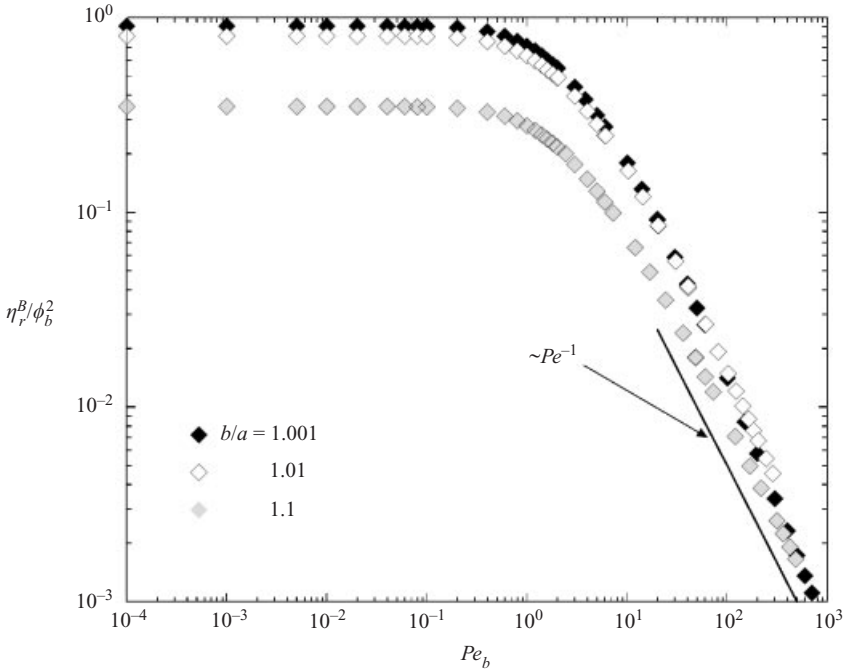

FIGURE 17. The Brownian contribution to the ϕ_b^2-coefficient of the relative viscosity as a function of Pe_b and b/a.

remains active also beyond the region of shear thinning; the microstructure is distorted faster by the imposed flow than Brownian motion can restore isotropy.

In figure 17, the $O(\phi_b^2)$ Brownian contribution to the relative shear viscosity has been isolated as a function of Pe_b, and excluded volume parameter b/a. The Brownian component decreases monotonically. At large Pe_b, the decrease is proportional to Pe_b^{-1}, although we note a somewhat faster decay for suspensions closer to the hard-sphere limit. This Pe_b-scaling of the Brownian viscosity is predicted by the theory of Brady & Morris (1997), and it is also in fair agreement with Stokesian dynamics simulations of concentrated suspensions (Foss & Brady 2000*b*). Since the Péclet number is the ratio of the relaxation time for diffusion to that of convection, Brownian motion cannot restore the microstructure at the same rate the flow distorts it and the Brownian viscosity shear thins at intermediate Pe_b. For large Pe_b, the rate of structural recovery by Brownian motion saturates in the boundary layer, which leads to a Pe_b^{-1} scaling of the Brownian viscosity (Brady & Morris 1997; Foss & Brady 2000*b*).

At small Pe_b, the initial departure from the Newtonian plateau is determined by the Brownian component in figure 17 for $b/a \approx 1$, because the magnitude of the hydrodynamic variation is far smaller. On increasing b/a, the interparticle force contribution increases gradually at the expense of the Brownian and hydrodynamic viscosities, and for large b/a it is the dominant contribution. The calculations here show that the deviations of the Brownian and interparticle force contributions to the viscosity from their Newtonian values vary proportional to Pe_b^2 irrespective of b/a. Hence, for all b/a, the total viscosity shear thins proportional to Pe_b^2, which confirms the results of previous analyses (Brady & Vicic 1995; Lionberger 1998).

Earlier work (Dhont 1989), although it contained the first correct diagnosis of the

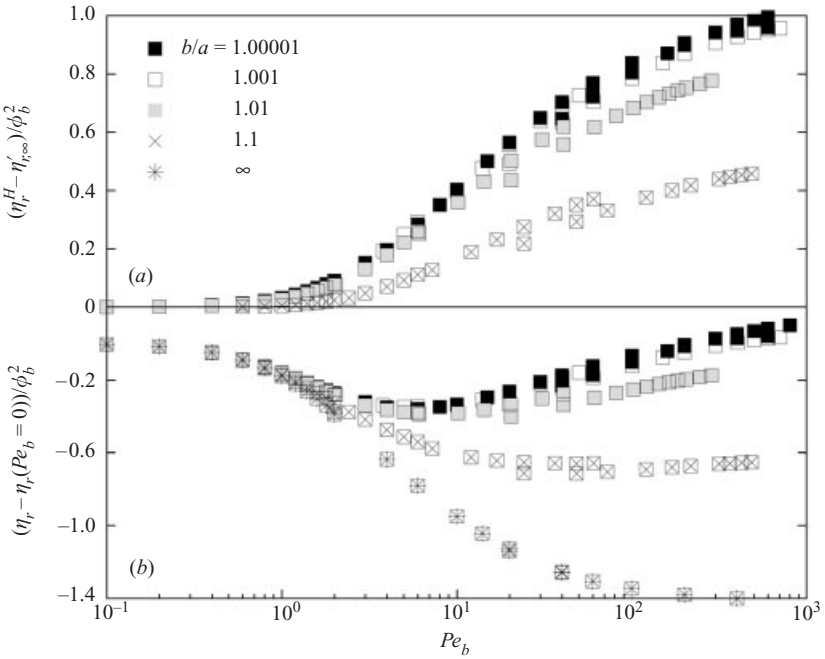

FIGURE 18. The ϕ_b^2-coefficient of (a) the hydrodynamic viscosity and (b) the total relative viscosity minus their small Pe_b values as functions of Pe_b and b/a.

Smoluchowski equation as being singularly perturbed at small Pe, concluded that shear thinning proceeds proportional to $Pe^{1/2}$. Subsequent numerical calculations (Blawzdziewicz & Szamel 1993) and experimental measurements (van der Werff, de Kruif & Dhont 1989*b*) appeared to support this result. However, the present analysis, together with the perturbation theory of Brady & Vicic (1995), should remove any question regarding the precise nature of shear thinning in dilute suspensions. Our results do show, however, that once the boundary-layer is well developed, the hard-sphere viscosity exhibits a regime of shear thinning where the decrease is approximately proportional to $Pe^{1/2}$. This occurs in the range $0.5 < Pe < 5$, which corresponds rather well with the results reported by Werff *et al.* (1989*b*) for the lowest volume fractions investigated.

As expected for large Pe_b and $b/a \approx 1$, the rheology is determined primarily by hydrodynamic interactions, whereas in the $b/a \to \infty$ limit the rheology is determined only by the interparticle force contribution. In the former case, Brownian motion plays a role only in so far as it affects the boundary-layer structure; as such, it is an indirect effect (see figure 17 showing that the direct contribution to the stress from Brownian motion is negligible at large Pe_b). At high shear rates, the viscosity can either enter into a region of continuous shear thickening or terminate in a large-Pe_b Newtonian plateau. The outcome is determined by the nature of the interparticle force.

For the excluded volume interaction considered in this work, the degree of shear thickening is modulated by the range of the excluded annulus. In figure 18(a) the deviation of the hydrodynamic viscosity from its small Pe_b value, given by the high-frequency dynamic viscosity η'_∞, is shown for varying b/a. The hydrodynamic viscosity at $O(\phi_b^2)$ is always an increasing function of Pe_b, but for shear thickening to occur

this increase must outweigh the decrease in the Brownian and interparticle force contributions. As seen from figure 18(*b*), where we show the shear rate dependence of the total viscosity less its small Pe_b value so that all curves start at zero for all values of b/a studied, this condition is fulfilled when $b/a \sim 1$; that is, shear thickening occurs only when particles are permitted to approach sufficiently close to experience the lubrication part of the hydrodynamic interaction. Although this information can be gleaned from the data in figure 11, this plot shows clearly the effect of the excluded volume parameter, and therefore hydrodynamics, on the shear thickening. As $b/a \to 1$ shear thickening occurs sooner and the magnitude increases. Both of these observations are in accord with simulation and experiment. These results also suggest that adding some degree of steric stabilization, e.g. through the addition of adsorbing surfactant or surface-grafting of polymer, may be an effective means for eliminating, or at least for postponing, the onset of shear thickening (see, e.g. Mewis & Biebaut 2001). However, the situation is likely to be more complicated because steric layers give rise to soft interactions and they will also affect the hydrodynamic interactions among particles (Potanin & Russel 1995).

The large accumulation of density near particle contact in the boundary-layer was noted early on in Stokesian dynamics simulations. In these concentrated systems the presence of the boundary-layer manifests itself in cluster formation at large Pe, and it was this cluster growth that was put forth as the mechanism causing shear thickening. This explanation was in conflict with the order–disorder transition to which Hoffman (1972) had earlier attributed the onset of shear thickening. In a recent view of the state of affairs concerning the origin of shear thickening, Hoffman (1998) maintains that the disruption of an ordered microstructure causes shear thickening. The latest Stokesian dynamics simulation study of concentrated Brownian hard spheres reports no evidence of structural ordering (Foss & Brady 2000*b*). The simulation results, together with the present two-particle results on systems that intrinsically lack any structural order, provide conclusive evidence for shear thickening being triggered by the interplay between hydrodynamic lubrication interactions and boundary-layer formation. Finally, experimental techniques that can resolve the hydrodynamic and Brownian contributions to the viscosity also conclude that shear thickening is driven by hydrodynamic interactions (Bender & Wagner 1996; Kaffashi *et al.* 1997; O'Brien & Mackay 2000).

Barnes (1989) proposes that shear thickening – albeit perhaps not to a degree measurable mechanically – will occur in all suspensions. The present analysis demonstrates that this conclusion will probably hold provided particles are not hindered from approaching close to physical contact where hydrodynamic lubrication interactions come into play. In this study, shear thickening was removed by keeping particle pairs apart, accomplished through an infinite repulsive force, which is, as such, rather unrealistic. We may expect that repulsive interparticle interactions cannot withstand the compressive hydrodynamic forces at large Pe and thus cannot prevent a boundary-layer from forming near particle contact. Nevertheless, the results of the study of the excluded volume interaction point to the importance of the competition between interparticle and hydrodynamic interactions at large Pe. Such a competition is the argument used by Boersma, Laven & Stein (1990) in suggesting a simple criterion for locating the shear-thickening regime in non-hard-sphere suspensions, although the method by which the result is obtained has been criticized (Marrucci & Denn 1985). Computer simulations have been used to demonstrate clearly that the form of the interparticle potential affects the degree of shear thickening (Catherall, Melrose & Ball 2000).

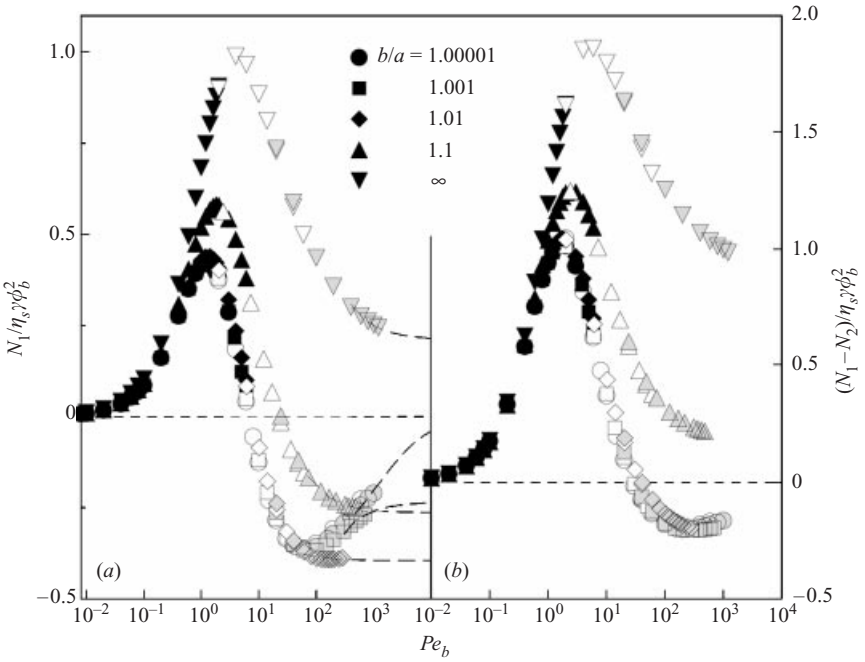

FIGURE 19. (*a*) The first normal stress difference and (*b*) the difference between the first and second normal stress differences at $O(\phi_b^2)$ as functions of Pe_b and excluded volume parameter b/a. Filled black symbols, surface spherical harmonic expansion; open symbols, finite-difference solution; tinted symbols, finite-difference solution of the boundary-layer equation; dashed lines, extrapolation of large Pe_b results.

Shear thickening is a well-documented effect in strongly sheared colloidal suspensions. The lubrication interactions that cause shear thickening also bring about a second important effect in strong flows: the sign reversal of the first normal stress difference on going from small to large Pe. Figure 19 summarizes the $O(\phi_b^2)$ results for N_1 and $N_1 - N_2$ as functions of Pe_b and b/a. The dominant transport mechanism at small Pe_b (and not too large b/a) is Brownian motion, which dictates that $N_1 > 0$. On increasing Pe_b hydrodynamic interactions gradually overcome Brownian motion, aside from the balance that exists in the boundary-layer, which leads to $N_1 < 0$. Increasing b/a simply moves the boundary-layer away from particle-particle contact, which has two connected effects. As shown in figures 9 and 10, the boundary-layer structure changes such that the boundary-layer asymmetry decreases with increasing b/a. In addition, on increasing b/a the particles no longer experience lubrication interactions, and for $b/a \to \infty$ the influence of hydrodynamic interactions vanishes entirely. The former effect dictates that the $Pe \to \infty$ and $b/a \to \infty$ limit of N_1 is small and positive, whereas the combination of the two prevents the sign reversal from occurring at large b/a.

In figure 19 we have extrapolated the large Pe_b results to the $Pe_b \to \infty$ limit. This was done by assuming the following asymptotic form: $N_1 \approx \alpha + Pe_b^{-1}\beta$, where the b/a-dependent coefficients α and β were obtained from a linear least-squares analysis of $Pe_b N_1$ versus Pe_b plots. The $b/a \to \infty$ results in figure 19 qualitatively agree with those from Brownian dynamics simulations of concentrated hard sphere suspensions (Foss & Brady 2000*a*). N_1 is positive for all Pe and the maximum at $Pe \sim O(1)$ is reproduced. Note, however, that for Pe beyond $O(10)$ the concentrated

suspensions form ordered structures in the flow when hydrodynamic interactions are absent, which precludes making any comparisons with the large Pe results from the present study. There are some data on concentrated suspensions of electrostatically stabilized particles that support some of the normal stress findings reported here. The polyvinyl chloride suspensions studied by Jomha & Reynolds (1993) exhibit the initial $N_1 \propto Pe^2$ behaviour and a sublinear Pe dependence at larger Pe, which would appear as a maximum when the normalization in figure 19 is used. The situation is, however, less clear for the other suspensions they examined.

In experimental measurements of normal stresses Zarraga, Hill & Leighton (2000) recently determined that N_1 is negative for concentrated suspensions of non-colloidal spheres. Moreover, they found $(N_1 - N_2)/\eta_s > 0$ and that it is roughly a linear function of shear rate. The large Pe_b results in figure 19 are only in qualitative accord with these experimental results if we assign a small excluded volume repulsion ($b/a \sim 1.1$) to the interactions among the glass spheres in the experiments. Note, however, that such a repulsive range is large in absolute terms since the particles are several tens of micrometres; we may thus have to look for an alternative explanation to the one given here, such as the role of concentration, inertia or polydispersity. For this range of repulsion the Brownian contribution to the normal stresses is negligible, and they are determined essentially only by hydrodynamic and interparticle forces, as is probably the case in the experiments. Figure 19 shows then that $(N_1 - N_2)/\eta_s \dot{\gamma} \phi_b^2 > 0$ and that it asymptotes to a finite positive value. It follows that $(N_1 - N_2)/\eta_s$ will be a nearly linear function of shear rate, as observed experimentally.

Non-Newtonian effects in dilute colloidal suspensions are difficult to detect mechanically. Therefore, measurements are usually conducted on concentrated suspensions, which are of course also of greater technical and industrial relevance. Simple scaling analyses in past works have yielded approximate but useful correlations for the rheological and diffusional properties of colloidal suspensions. For example, it was recently shown that the shear thinning Brownian part of the viscosity from Stokesian dynamics simulations of concentrated hard sphere suspensions could be reduced to a concentration independent correlation using the long-time self-diffusivity (Foss & Brady 2000*b*). A similar treatment can be used to extend the dilute Brownian viscosity calculated here to high concentrations.

Shear thickening is expected to be particularly well-captured by a scaling analysis since pair interactions should dominate even in a concentrated suspension. The squeezing together of the pair is resisted only by the pure solvent, leaving the lubrication interaction essentially unaltered from that between the isolated pairs in this study. Supported by a previous scaling analysis of Stokesian dynamics simulations results (Foss & Brady 2000*b*), we expect that the influence of a third or more particles on this strong pair interaction should be captured by a mean-field treatment, e.g. through a renormalization of the the surrounding solvent viscosity to the high-frequency dynamic viscosity η'_∞ at the concentration of interest. The scaling analysis of the present results will be presented elsewhere.

We can now claim that the origin of continuous shear thickening is fully understood; it arises because of boundary-layer formation at small interparticle separations. It is thus reasonable to expect the degree of shear thickening to be decreased in concentrated suspensions by maintaining particles well separated, which provides a rationale for designing suitable surface modifications. A second important effect caused by the boundary-layer is a sign reversal in the first normal stress difference, which assumes negative values in strong shear flows because the lubrication forces act to preserve the boundary-layer in the extensional zone. The present results for

dilute, model colloidal suspensions in both weak and strong shear flows, which show that they behave qualitatively the same as concentrated suspensions, provide a firm basis for analysing the role of colloidal forces on the rheological behaviour.

This work was supported in part by a grant from IFPRI.

Appendix A. The non-equilibrium osmotic pressure

In this Appendix we re-examine the determination of the osmotic pressure. The expressions for the stresses can be cast in different, equivalent forms; the specific choice made is based generally on convenience. Here we choose the original formulation due to Batchelor (1977). The two-body expressions for the thermodynamic stresses are

$$\frac{\langle \boldsymbol{S}^P \rangle}{nkT} = -\frac{1}{2}\int \mathrm{d}\boldsymbol{r} g(\boldsymbol{r})(\boldsymbol{rF} + 2\boldsymbol{C}\cdot\boldsymbol{F}), \tag{A 1}$$

$$\frac{\langle \boldsymbol{S}^B \rangle}{nkT} = -\int_{r=2a} \mathrm{d}A\, g(2a\boldsymbol{n})(a\boldsymbol{nn} + \boldsymbol{C}\cdot\boldsymbol{n}) - \int \mathrm{d}\boldsymbol{r} g(\boldsymbol{r})\nabla\cdot\boldsymbol{C} + \int_{r\to\infty} \mathrm{d}A\boldsymbol{C}\cdot\boldsymbol{n}, \tag{A 2}$$

where $\mathrm{d}A = r^2\mathrm{d}\Omega$ and $\boldsymbol{C} = (\boldsymbol{R}_{SU}\cdot\boldsymbol{R}_{FU}^{-1})_2 + (\boldsymbol{R}_{SU}\cdot\boldsymbol{R}_{FU}^{-1})_1$ is not traceless in its first two Cartesian indices; instead,

$$\boldsymbol{C} = \tilde{\boldsymbol{C}} + \tfrac{1}{3}\boldsymbol{I}(\boldsymbol{I}:\boldsymbol{C}) = \tilde{\boldsymbol{C}} + \boldsymbol{IA}, \tag{A 3}$$

where $A^\alpha = \frac{1}{3}\delta^{\beta\gamma}C^{\beta\gamma\alpha}$ and $\tilde{C}^{\beta\gamma\alpha}$ is the traceless part of $C^{\beta\gamma\alpha}$.

Since $\tilde{\boldsymbol{C}}\cdot\boldsymbol{n} \to -a(\boldsymbol{nn} - \frac{1}{3}\boldsymbol{I})$ and $\boldsymbol{A} \to -\frac{1}{3}a\boldsymbol{n}$ as $r \to 2a$, the first term in the Brownian stress vanishes, leaving

$$\frac{\langle \boldsymbol{S}^B \rangle}{nkT} = -\frac{1}{2}\int \mathrm{d}\boldsymbol{r} g(\boldsymbol{r}) W(r)\left(\hat{\boldsymbol{r}}\hat{\boldsymbol{r}} - \tfrac{1}{3}\boldsymbol{I}\right) - \boldsymbol{I}\int \mathrm{d}\boldsymbol{r} g(\boldsymbol{r})\nabla\cdot\boldsymbol{A} + \int_{r\to\infty} \mathrm{d}A\boldsymbol{C}\cdot\boldsymbol{n}, \tag{A 4}$$

where $\nabla\cdot\tilde{\boldsymbol{C}} = \frac{1}{2}W(r)\left(\hat{\boldsymbol{r}}\hat{\boldsymbol{r}} - \frac{1}{3}\boldsymbol{I}\right)$. The term containing the hydrodynamic function $\boldsymbol{A} = -\frac{2}{9}a\mathscr{A}(r)\hat{\boldsymbol{r}}$, with $\mathscr{A}(r)$ decaying as $\frac{3}{2}\left(\frac{a}{r}\right)^2$ in the far field (Jeffrey *et al.* 1993), is not absolutely convergent. This is resolved by writing $g(\boldsymbol{r})\nabla\cdot\boldsymbol{A} = \nabla\cdot(\boldsymbol{A}g(\boldsymbol{r})) - \boldsymbol{A}\cdot\nabla g(\boldsymbol{r})$, which results in

$$-\boldsymbol{I}\int \mathrm{d}\boldsymbol{r}\nabla\cdot(\boldsymbol{A}g(\boldsymbol{r})) + \boldsymbol{I}\int \mathrm{d}\boldsymbol{r}\boldsymbol{A}\cdot\nabla g(\boldsymbol{r}) + \boldsymbol{I}\int_{r\to\infty} \mathrm{d}A\,\boldsymbol{A}\cdot\boldsymbol{n}, \tag{A 5}$$

where we have eliminated the traceless part of $\boldsymbol{C}$ in the last term by completing the angular integrations. The divergence theorem eliminates further the surface integrals in the far field, and the remaining terms provide us with a convergent expression for the Brownian stress

$$\frac{\langle \boldsymbol{S}^B \rangle}{nkT} = -\frac{1}{2}\int \mathrm{d}\boldsymbol{r} g(\boldsymbol{r}) W(r)\left(\hat{\boldsymbol{r}}\hat{\boldsymbol{r}} - \tfrac{1}{3}\boldsymbol{I}\right) + \boldsymbol{I}\int_{r=2a} \mathrm{d}A\,\boldsymbol{A}\cdot\boldsymbol{n}g(2a\boldsymbol{n}) + \boldsymbol{I}\int \mathrm{d}\boldsymbol{r}\boldsymbol{A}\cdot\nabla g(\boldsymbol{r}). \tag{A 6}$$

Since we treat systems with a hard core repulsion at $r = 2b > 2a$, the surface integral in the above vanishes owing to $g(\boldsymbol{r})$ being zero for $r < 2b$, which is the reason it does not appear in (3.7) quoted earlier.

For a hard-sphere suspension at equilibrium only the middle term in (A 6) survives. Hence, the Brownian stress alone determines the osmotic pressure (Brady 1993). For the excluded volume interaction in (2.5), however, it is the interparticle stress that determines the osmotic pressure through the force $\boldsymbol{F} = kT\delta(r - 2b)\hat{\boldsymbol{r}}$.

Out of equilibrium, it is convenient to combine the parts of the interparticle and Brownian stresses that involve the trace of $\mathbf{C}$ by using the identity

$$g(\boldsymbol{r})\boldsymbol{A}\cdot\left(\nabla\ln g(\boldsymbol{r})+\frac{1}{kT}\nabla V(r)\right)=\mathrm{e}^{-V(r)/kT}\boldsymbol{A}\cdot\nabla\left(\frac{g(\boldsymbol{r})}{\mathrm{e}^{-V(r)/kT}}\right), \tag{A 7}$$

which leads to the last term in the Brownian stress in (3.7). Note that this term is finite for hard spheres, for which $V(r)=0$, and should accordingly be interpreted as a stress contribution from Brownian motion.

Appendix B. Boundary-layer equation

Combining (2.6) with the two-body expressions for the diffusivity tensor and the relative particle velocity, the two-body Smoluchowski equation assumes the following form

$$\begin{aligned}\frac{1}{r^2}\frac{\partial}{\partial r}\left(r^2G\frac{\partial g}{\partial r}\right)+\frac{H}{r^2\sin\theta}\left(\frac{\partial}{\partial\theta}\left(\sin\theta\frac{\partial g}{\partial\theta}\right)+\frac{1}{\sin\theta}\frac{\partial^2 g}{\partial\varphi^2}\right)\\ =\frac{Pe_b}{2}\left(gW\gamma_r+r(1-A)\gamma_r\frac{\partial g}{\partial r}+(\gamma_\theta-Be_\theta)\frac{\partial g}{\partial\theta}+\frac{(\gamma_\varphi-Be_\varphi)}{\sin\theta}\frac{\partial g}{\partial\varphi}\right),\end{aligned} \tag{B 1}$$

where γ_r, γ_θ, and γ_φ are components of the velocity vector $\langle\hat{\boldsymbol{\Gamma}}\rangle\cdot\hat{\boldsymbol{r}}$ in the spherical coordinate system depicted in figure 2. Also, $e_\theta=\hat{\boldsymbol{r}}\cdot\langle\hat{\boldsymbol{E}}\rangle\cdot\hat{\theta}$ and $e_\varphi=\hat{\boldsymbol{r}}\cdot\langle\hat{\boldsymbol{E}}\rangle\cdot\hat{\varphi}$. For the simple shear flow with $\langle\hat{\boldsymbol{\Gamma}}\rangle=\hat{\boldsymbol{z}}\hat{\boldsymbol{x}}$ under consideration here, they are given by

$$\gamma_r=\sin\theta\cos\theta\cos\varphi,\quad \gamma_\theta=-\sin^2\theta\cos\varphi,\quad \gamma_\varphi=0, \tag{B 2}$$

$$e_\theta=\tfrac{1}{2}(\gamma_\theta+\cos^2\theta\cos\varphi),\quad e_\varphi=-\tfrac{1}{2}\cos\theta\cos\varphi. \tag{B 3}$$

To focus on the behaviour of the boundary layer, we stretch the radial coordinate by defining $y=Pe_b(r-2)$. Dividing both sides of (B 1) by Pe_b^2, we obtain the following equation

$$\begin{aligned}G\frac{\partial^2 g}{\partial y^2}+Q\frac{\partial g}{\partial y}+\frac{HPe_b^{-2}}{4\sin\theta}\left(\frac{\partial}{\partial\theta}\left(\sin\theta\frac{\partial g}{\partial\theta}\right)+\frac{1}{\sin\theta}\frac{\partial^2 g}{\partial\varphi^2}\right)+O(Pe_b^{-3})\\ =\frac{Pe_b^{-1}}{2}\left(gW\gamma_r+(\gamma_\theta-Be_\theta)\frac{\partial g}{\partial\theta}+\frac{(\gamma_\varphi-Be_\varphi)}{\sin\theta}\frac{\partial g}{\partial\varphi}\right),\end{aligned} \tag{B 4}$$

where we have neglected terms of order Pe_b^{-3} and higher. The lowest-order term neglected is proportional to $y^2Pe_b^{-3}$, indicating that (B 4) is not uniformly valid for strong flows, but is valid only near particle contact ($y\sim 0$) where the boundary layer indeed exists in the compressional quadrant. The function Q in (B 4) is given by

$$Q=\frac{\mathrm{d}G}{\mathrm{d}y}+GPe_b^{-1}\left(1-\tfrac{1}{2}yPe_b^{-1}\right)-\gamma_r(1-A)\left(1+\tfrac{1}{2}yPe_b^{-1}\right). \tag{B 5}$$

The boundary conditions to be satisfied by (B 4) are given by

$$\gamma_r(1-A)g-G\frac{\partial g}{\partial y}=0,\quad y=0,\quad g\to 1,\quad y\to\infty, \tag{B 6}$$

By neglecting also the $O(Pe_b^{-2})$ terms, (B 4) reduces to the equation analysed by Brady & Morris (1997).

REFERENCES

Ackerson, B. J. 1990 Shear-induced order and shear processing of model hard sphere suspensions. *J. Rheol.* **34**, 553–590.

Barnes, H. A. 1989 Shear thickening (dilatancy) in suspensions of nonaggregating solid particles dispersed in Newtonian liquids. *J. Rheol.* **33**, 329–366.

Batchelor, G. K. 1977 The effect of Brownian motion on the bulk stress in a suspension of spherical particles. *J. Fluid Mech.* **83**, 97–117.

Batchelor, G. K. & Green, J. T. 1972 The determination of the bulk stress in a suspension of spherical particles to order c^2. *J. Fluid Mech.* **56**, 401–427.

Bender, J. & Wagner, N. J. 1995 Optical measurements of the contribution of colloidal forces to the rheology of concentrated suspensions. *J. Colloid Interface Sci.* **172**, 171–184.

Bender, J. & Wagner, N. J. 1996 Reversible shear thickening in monodisperse and bidisperse colloidal dispersions. *J. Rheol.* **40**, 899–916.

Bergenholtz, J. & Wagner, N. J. 1994 The Huggins coefficient for the square-well colloidal fluid. *Ind. Engng Chem. Res.* **33**, 2391–2397.

Berry, D. H. & Russel, W. B. 1987 The rheology of dilute suspensions of slender rods in weak flows. *J. Fluid Mech.* **180**, 475–494.

Blawzdziewicz, J. & Szamel, G. 1993 Structure and rheology of semidilute suspensions under shear. *Phys. Rev.* E **48**, 4632–4636.

Boersma, W. H., Laven, J. & Stein, H. N. 1990 Shear thickening (dilatancy) in concentrated dispersions. *AIChE J.* **36**, 321–332.

Bossis, G. & Brady, J. F. 1989 The rheology of Brownian suspensions. *J. Chem. Phys.* **91**, 1866–1874.

Brady, J. F. 1993 Brownian motion, hydrodynamics, and the osmotic pressure. *J. Chem. Phys.* **98**, 3335–3341.

Brady, J. F. 1996 Model hard-sphere dispersions: statistical mechanical theory, simulations, and experiments. *Curr. Opinion Colloid Interface Sci.* **1**, 472–480.

Brady, J. F. & Morris, J. F. 1997 Microstructure of strongly sheared suspensions and its impact on rheology and diffusion. *J. Fluid Mech.* **348**, 103–139.

Brady, J. F. & Vicic, M. 1995 Normal stresses in colloidal dispersions. *J. Rheol.* **39**, 545–566.

Catherall, A. A., Melrose, J. R. & Ball, R. C. 2000 Shear-thickening and order–disorder effects in concentrated colloids at high shear rates. *J. Rheol.* **44**, 1–25.

Dhont, J. K. G. 1989 On the distortion of the static structure factor of colloidal fluids in shear flow. *J. Fluid Mech.* **204**, 421–431.

Foss, D. R. & Brady, J. F. 2000*a* Brownian dynamics simulations of hard-sphere colloidal dispersions. *J. Rheol.* **44**, 629–651.

Foss, D. R. & Brady, J. F. 2000*b* Structure, diffusion and rheology of Brownian suspensions by Stokesian dynamics simulation. *J. Fluid Mech.* **407**, 167–200.

Hoffman, R. L. 1972 Discontinuous and dilatant viscosity behaviour in concentrated suspensions. I. Observation of a flow instability. *Trans. Soc. Rheol.* **16**, 155–173.

Hoffman, R. L. 1998 Explanations for the cause of shear thickening in concentrated colloidal suspensions. *J. Rheol.* **42**, 111–123.

Jeffrey, D. J., Morris, J. F. & Brady, J. F. 1993 The pressure moments for two rigid spheres in low-Reynolds-number flow. *Phys. Fluids* A **5**, 2317–2325.

Jomha, A. I. & Reynolds, P. A. 1993 An experimental study of the first normal stress difference–shear stress relationship in simple shear flow for concentrated shear thickening suspensions. *Rheol. Acta* **32**, 457–464.

Kaffashi, B., O'Brien, V. T., Mackay, M. E. & Underwood, S. M. 1997 Elastic-like and viscous-like components of the shear viscosity for nearly hard sphere Brownian suspensions. *J. Colloid Interface Sci.* **187**, 22–28.

Lionberger, R. A. 1998 Shear thinning of colloidal dispersions. *J. Rheol.* **42**, 843–863.

Lionberger, R. A. & Russel, W. B. 1994 High frequency modulus of hard sphere colloids. *J. Rheol.* **38**, 1885–1908.

Lionberger, R. A. & Russel, W. B. 2000 Microscopic theories of the rheology of stable colloidal dispersions. *Adv. Chem. Phys.* **111**, 399–474.

McQuarrie, D. A. 1983 *Quantum Chemistry*. University Science Books.

Marrucci, G. & Denn, M. M. 1985 On the viscosity of a concentrated suspension of solid spheres. *Rheol. Acta* **24**, 317–320.

Mewis, J. & Biebaut, G. 2001 Shear thickening in steady and superposition flows effect of particle interaction forces. *J. Rheol.* **45**, 799–813.

Mewis, J., Frith, W. J., Strivens, T. A. & Russel, W. B. 1989 The rheology of suspensions containing polymerically stabilized particles. *AIChE J.* **35**, 415–422.

Ng, K.-C. 1974 Hypernetted chain solutions for the classical one-component plasma up to $\Gamma = 7000$. *J. Chem. Phys.* **61**, 2680–2689.

O'Brien, V. T. & Mackay, M. E. 2000 Stress components and shear thickening of concentrated hard sphere suspensions. *Langmuir* **16**, 7931–7938.

Parsi, F. & Gadala-Maria, F. 1987 Fore-and-aft asymmetry in a concentrated suspension of solid spheres. *J. Rheol.* **31**, 725–732.

Phung, T. N., Brady, J. F. & Bossis, G. 1996 Stokesian dynamics simulation of Brownian suspensions. *J. Fluid Mech.* **313**, 181–207.

Potanin, A. A. & Russel, W. B. 1995 Hydrodynamic interaction of particles with grafted polymer brushes and applications to rheology of colloidal dispersions. *Phys. Rev.* E **52**, 730–737.

Press, W. H., Teukolsky, S. A., Vetterling, W. T. & Flannery, B. P. 1992 *Numerical Recipes in FORTRAN*, 2nd edn. Cambridge University Press.

Russel, W. B. 1978 The rheology of charged rigid spheres. *J. Fluid Mech.* **85**, 209–232.

Russel, W. B. 1980 Review of the role of colloidal forces in the rheology of suspensions. *J. Rheol.* **24**, 287–317.

Russel, W. B. 1984 The Huggins coefficient as a means for characterizing suspended particles. *J. Chem. Soc. Faraday Trans. 2* **80**, 31–41.

Russel, W. B., Saville, D. A. & Schowalter, W. R. 1989 *Colloidal Dispersions.* Cambridge University Press.

Segre, P. N., Meeker, S. P., Pusey, P. N. & Poon, W. C. K. 1995 Viscosity and structural relaxation in suspensions of hard-sphere colloids. *Phys. Rev. Lett.* **75**, 958–961.

Vicic, M. 1999 Rheology and microstructure of complex liquids: Dispersions, emulsions and polymer solutions. PhD dissertation, California Institute of Technology.

Watanabe, H., Yao, M.-L., Osaki, K., Shikata, T., Niwa, H. & Morishima, Y. 1999 Nonlinear rheology of concentrated spherical silica dispersions: 3. Concentration dependence. *Rheol. Acta* **38**, 2–13.

van der Werff, J. C., de Kruif, C. G., Blom, C. & Mellema, J. 1989*a* Linear viscoelastic behaviour of dense hard sphere dispersions. *Phys. Rev.* A **39**, 795–807.

van der Werff, J. C., de Kruif, C. G. & Dhont, J. K. G. 1989*b* The shear-thinning behaviour of colloidal dispersions. II. Experiments. *Physica* A **160**, 205–212.

Wilson, H. & Davis, R. H. 2000 The viscosity of a dilute suspension of rough spheres. *J. Fluid Mech.* **421**, 339–367.

Yan, Y. D. & Dhont, J. K. G. 1993 Shear-induced structure distortion in nonaqueous dispersions of charged colloidal spheres via light scattering. *Physica* A **198**, 78–107.

Zarraga, I. E., Hill, D. A. & Leighton, D. T. 2000 The characterization of the total stress of concentrated suspensions of noncolloidal spheres in Newtonian fluids. *J. Rheol.* **44**, 185–220.

Zarraga, I. E. & Leighton, D. T. 2001 Normal stress and diffusion in a dilute suspension of hard spheres undergoing simple shear. *Phys. Fluids* **13**, 565–577.